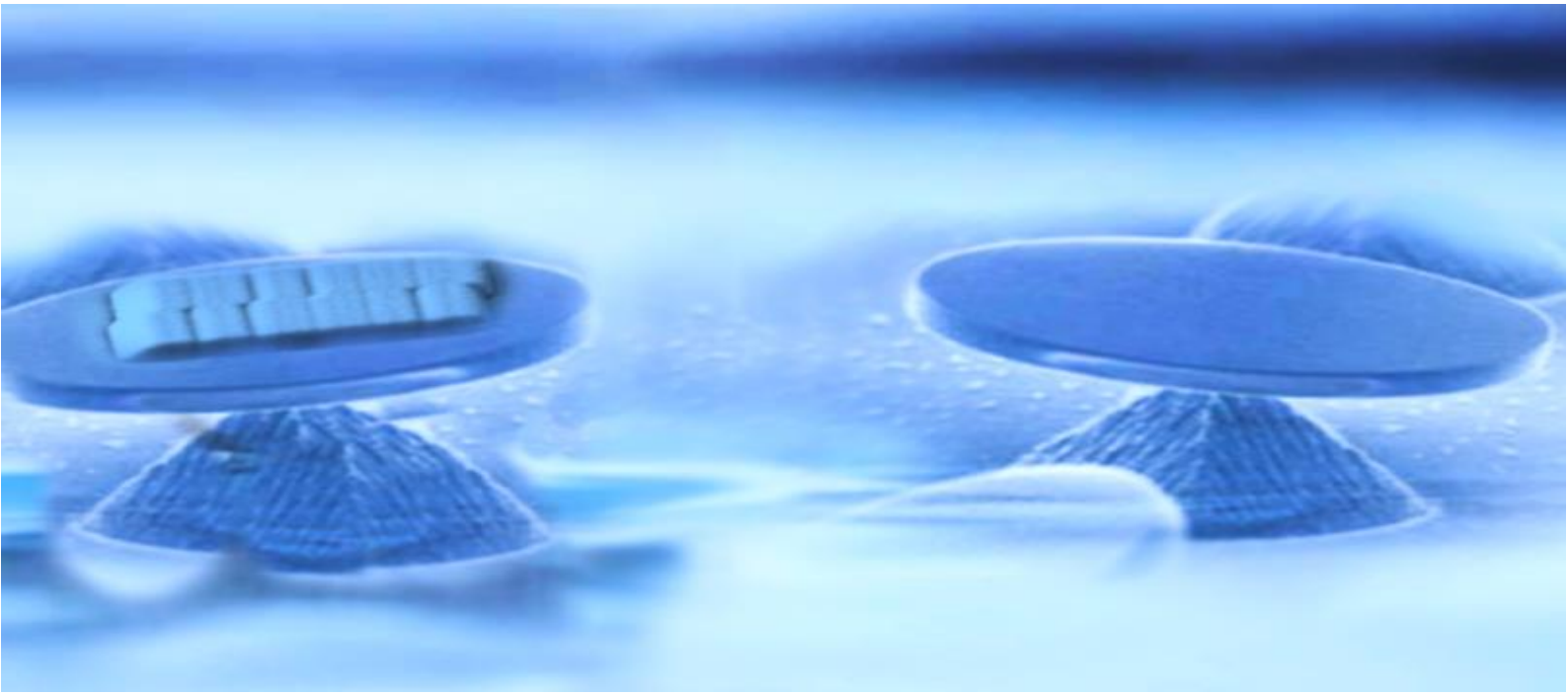

Optical metasurfaces for momentum exchange between light and matter

Mahdi Shanei

DEPARTMENT OF PHYSICS

CHALMERS UNIVERSITY OF TECHNOLOGY

Gothenburg, Sweden 2023

www.chalmers.se

THESIS FOR THE DEGREE OF LICENTIATE OF TECHNOLOGY

Optical metasurfaces for momentum exchange between light and matter

Mahdi Shanei

CHALMERS
UNIVERSITY OF TECHNOLOGY

Department of Physics
Chalmers University of Technology
Göteborg, Sweden, 2023

Optical metasurfaces for momentum exchange between light and matter

Mahdi Shanei

Division of Nano- and biophysics
Department of Physics
Chalmers University of Technology
SE-412 96 Gothenburg
Sweden
Telephone + 46 (0)31-772 1000

Cover:
Left: A rotary meta-particle with embedded gratings that deflect light in opposite directions.
Right: A passive particle.

Printed. In Sweden by
Chalmers digital printing
Chalmers Tekniska Högskola
Gothenburg, Sweden 2023

CHALMERS UNIVERSITY OF TECHNOLOGY

Department of Physics

Optical metasurfaces for momentum exchange between light and matter

Mahdi Shanei

Abstract

Light carries energy and momentum that can be transferred to matter. Because of the conservation of total momentum, a change in light momentum due to interaction with an object must be compensated by an equal but opposite change in the momentum of that object. The resulting optical forces may in turn cause observable mechanical translation and rotation of the object, as a consequence of a change in linear and angular momentum of the light, respectively. These effects can be controlled by structuring the impinging light field and/or by engineering the optical properties of the object.

Metasurfaces, flat structures with engineered subwavelength building blocks, provide various possibilities for tailoring optical forces and momentum exchange. A metasurface can be used as a compact replacement for conventional bulky optical elements used to shape light, such as lenses and spatial light modulators. An example of this is provided in the appended paper, where a cylindrical metalens with a linear phase gradient is used to optically trap and translate small particles along its line focus. But in the process of shaping a light beam, a metasurface is itself subject to momentum exchange and optical forces. This effect can be observed if a metasurface is incorporated into a micro-scale object allowed to move freely across a surface. Several examples of such meta-particles propelled by light are provided in the thesis.

The thesis is organized as follows: The first part is devoted to studying the fundamentals and developments of optical metasurfaces by categorizing them based on aspects of material composition, working wavelength, and applications. Then a brief review of different actuation mechanisms used for the manipulation of micro and nano-objects is provided, with a focus on using optical fields as the external source of energy and momentum. The second part of the thesis is dedicated to results that highlight the versatility of stationary and movable metasurfaces in facilitating optical manipulation of objects. Finally, a description of the metasurface fabrication and characterization methods used is provided.

Keywords: Flat optics, phase-gradient metasurface, optical forces and torques, optical momentum exchange, meta-particle, rotary meta-motor, particle transport.

List of publications

The following paper is included in this thesis

---

i. Light-driven transport of microparticles with phase-gradient metasurfaces

Shanei, Mohammad Mahdi, Einstom Engay, and Mikael Käll.

Optics Letters 47, no. 24 (2022): 6428-6431.

Declaration of author contributions:

i: I did the nanofabrication, optimization and design of metasurface, numerical simulation, and wrote the first draft of the manuscript.

Acknowledgments

To my lovely parents. I owe a tremendous debt of gratitude and my appreciation is beyond words.

To my beloved Sepide and Jana because you are the best.

Mikael. I am deeply grateful for giving me the opportunity to be here, for your extensive support and for always keeping your door open. I could not imagine a better supervisor.

Pani. You are an inestimable friend and best companion to share this journey. Thanks for everything.

Tom. Thanks for your huge support. Without your help, I would have been stuck with measurements and other things. Congrats on your engagement, bud.

Daniel. Thanks for getting me started with my career and project. I am lucky that I have your constant advice and so happy to see your beautiful family, hope the best for you and the girls.

Emelie, Vasilii, Mindaugas, Hana and Ludwig. I am super fortunate to be in this group with you, guys. It is really difficult to see the group without any of you. Cheers on our Monday meetings.

Betül, Adri, Gosha. I am truly blessed to have such amazing friends. Many thanks for the kindness, support and energy you spread around.

Gan. The MEMS boy, I really do enjoy working with you on our shared project. I am looking forward to seeing your achievements very soon.

Ruggero. I appreciate you teaching me nanofabrication. You have always been positive and supportive.

Timur, Abhay, Sasha, Oleg, Ximin, Steven, Santosh, Peter Johansen, Battulga, Sebastian, and everyone else I have been so lucky to know you.

Many thanks to Alex, Sara, Ankit, Srdjan, Mahdad, Niclas and all people working at Myfab Chalmers for your valuable support and guidance.

Special thanks to Eva Olsson for her support, Philippe Tassin and Giovanni Volpe for their ideas and suggestions.

Contents

Chapter 1

Introduction

The quest to interpret our observation from optical phenomena boils down to understanding the light-matter interaction. Material science has a significant impact on the spread of interdisciplinary fields, including optics. Starting from bronze and iron to the revolutionary years of semiconductor discovery, materials science has often been an indispensable tool for the improvement of human life quality. When a natural material interacts with light, the behavior of the material can be described by the absorption and scattering of light. For example, the color of a butterfly's wings comes from the traditional chemical pigments, which reflect and absorb only a range of wavelengths. However, these melanin pigments are the natural elements that define an ordinary color. There is another type of light-wing interaction that relies on structural color. Butterflies' wings have different layers that are composed of periodic protein patterns. While the light travels through these layers, it can bounce and be partially reflected from them, usually appearing as iridescent blue [1].

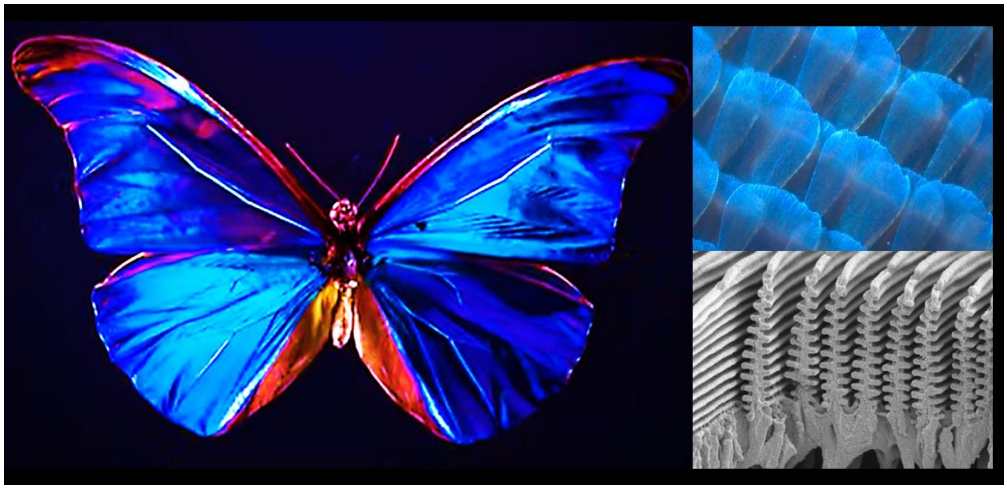

Figure 1.1: Natural and structural color of butterfly's wing from melanin pigments and multi-layers of protein patterns shown in the insets [1].

Similar to butterfly wings, the metamaterial is a new type of material that can interact with light waves differently from conventional material. Their building block is comprised of artificial subwavelength element building block which is patterned in three dimensions [2]. Recently, a two-dimensional version of metamaterial has gained a great deal of attention, mainly due to fabrication issues such as the possibility of large-scale fabrication. Moreover, contrary to metamaterial, metasurfaces consist of optically thin arrays of elements. Hence, their fabrication process is compatible with conventional CMOS technology and suitable for integration with other optical components [3]. The fundamental application of optical metasurfaces is within beam shaping or structuring the wavefront of light. These flat surfaces can manipulate different degrees of freedom of the light, including wavelengths, polarization, amplitude, and phase. Chapter 2 of this thesis is dedicated to studying the development of optical metasurfaces by categorizing them based on different aspects of constituted material, their phase coverage technique, design approaches, working wavelengths, active and passive types, and their applications. As a proof of concept, some of my results achieved by working on metasurfaces have been included in the related sections of this chapter.

When we can tailor a beam of light with metasurface, new possibilities to shape the optical force can be realized on a very compact scale. Optical forces are generated by momentum exchange between light and an object. Artur Ashkin used it for levitation and confinement of particles in 1976 [4], which brought him the physics Nobel prize in 2018. Maybe the first question that comes to our mind is, "How can light can exert force on an object?" or "From where does an optical force arise?". A concise answer is momentum! The answer to this question lies in another Noble prize in physics in 1921, where Einstein used Plank's theory to explain the

photoelectric effect. He introduced photons as quanta of energy of the light that can carry a well-defined momentum. Now, when a stream of millions of photons over time hits an object, the optical forces can arise from the transferred momenta to that object. Mechanical manipulation of objects, such as trapping, positioning, and sorting, has attracted interest in recent years with possible applications in therapy, drug delivery, sensing, and diagnosis [5], [6]. The prerequisite in the development of optical manipulation relies on the advances in the progress of optical forces and torques. Due to the various degrees of freedom of the optical waves, it is not surprising that this kind of actuation source can also be widely used to control objects at the micro and nanoscale. Therefore, metasurfaces can play an important role in precisely applying optical forces and facilitating different types of momentum exchanges between light and matter.

Chapter 3 begins with a brief introduction about different actuation mechanisms in the manipulation of micro and nano-objects and continues by focusing on the optical field as an external excitation source such as photochemical, photothermal, photomechanical, optoelectronics effects and finally, direct optical manipulation, which is enabled purely through light-matter momentum interaction without any secondary phenomena. In the last part of this chapter, the applications of metasurfaces have been studied in optical tweezers by investigating different possibilities that a metasurface can provide in momentum exchanges between light and matter. Chapter 4 presents the research methods, including numerical simulations, processes, and experimental optical setup used to reach the results of the appended paper. To conclude this thesis, Chapter 5 has been dedicated to a summary of the appended paper and the outlooks, highlighting the tracks for the continuation of this thesis in the future.

Chapter 2

Flat optics and metasurfaces

Beam shaping with refractive optical components is based on the gradual phase accumulation that is acquired through light propagation over a certain distance much larger than the effective wavelength of light. Fabricating these elements relies on precise surface polishing and alignment tools, which usually lead to bulky and expensive elements [7]. While diffractive optics with constitutive elements that are arranged at the scale of wavelength can be a suitable replacement for conventional bulky and heavy components, they suffer from unwanted propagation of different spurious diffraction orders. This can lead not only to noticeable degradation of the device's efficiency but also to the appearance of ghost and virtual focal points in imaging systems [8].

In the evolution of optical metasurfaces, three-dimensional metamaterials with engineered optical and electrical properties played an indispensable role. Metamaterials are artificially structured materials composed of sub-wavelength elements that can present some extraordinary behavior under external field excitation. In the optical field, this can usually be achieved through the spatial modification of the dielectric function of material (ε and μ) [2], [9]. To fulfill this kind of modification, the material should have a certain thickness to apply a gradual change in different components of the incident field. The thickness of metamaterial causes various drawbacks in their implementation to shape the light field, such as low efficiency and losses, fabrication constraints, and bulky nature [10], [11].

The advent of flat metasurfaces, a two-dimensional version of metamaterials, provides promising possibilities for tackling the conventional disadvantages of metamaterials. Metasurfaces consist of individual subwavelength elements, also called meta-atoms, that are patterned on a substrate [12]. Contrary to metamaterials, metasurfaces can introduce abrupt changes in the amplitude, phase, and polarization of incident wavefront with their ultra-thin thicknesses. Metasurfaces have the potential to provide a versatile platform for different applications and scopes in optics and photonics. Due to this, they have gained remarkable attention in the past decade. Some features such as multifunctional, tunability, flexibility in design, and high sensitivity make them a hot developing topic in the current literature of flat optics. In the following sections of this chapter, the development of metasurfaces has been studied by dividing them into different groups based on their properties and performance.

2.1. Full-phase coverage approaches

Conventional optical refractive elements such as lenses can shape the phase profile of the beam wavefront by introducing different spatial phase accumulations through a curved structure. In metasurfaces, the individual planar meta-atoms are responsible for providing 2π phase changes that are required to shape the wavefront. Various approaches have been used to introduce full 2π phase coverage by utilizing strong light-matter interactions between the building blocks of the metasurface and the incident wave. These techniques can be categorized into three main approaches, resonance, propagating, and geometrical or Pancharatnam Berry (PB) phases for dielectric metasurfaces. It is worth mentioning that there is also a hybrid technique combining the propagating and resonance phase methods. Figure 2.1 illustrates a schematic illustration of different techniques and the top view of decorated metasurfaces.

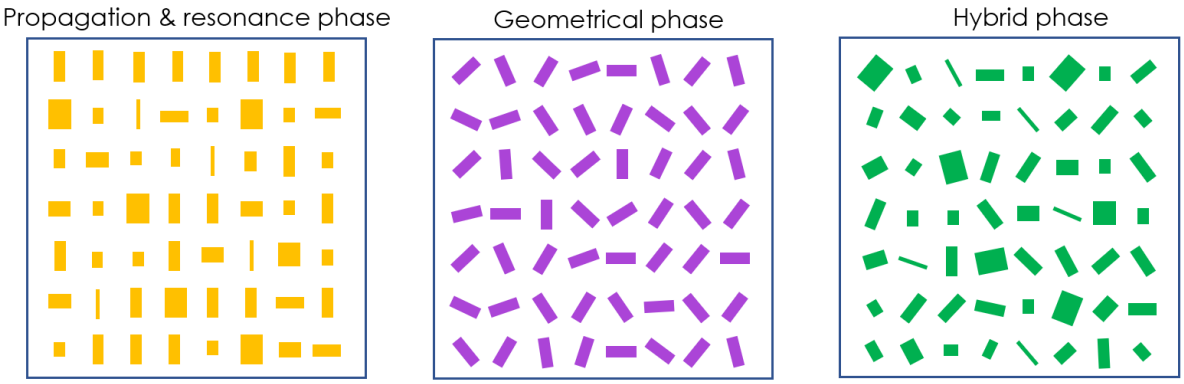

Figure 2.1: Three methods to print the required amplitude and phase modulation on a surface. Left: Different cross-sections have been used to engineer the effective refractive index of light. Meta-atoms in the propagation phase approach generally have a higher aspect ratio than the ones in resonance phases. Middle: Geometrical phase technique uses the rotation of a specific meta-atom in a plane perpendicular to the propagation of the incident light. Left: The hybrid phase approach combines geometrical and propagation techniques to simultaneously modulate the phase and amplitude of impinging beam [13].

2.1.1. Propagating phase

The ptopagating phase approach is based on the simple definition of the optical path length and the accumulated phase, where they vary proportionally with the refractive index of the medium. Hence, the building blocks in a metasurface can arbitrarily define the phase of extracted beams by modulation of the effective refractive index by varying the filling factors. The phase delays can be calculated by

$$\phi_{\mathrm{WG}} = \frac{2\pi}{\lambda} n_{\mathrm{eff}} H, \tag{2.1}$$

where λ, H and n_{eff} are the subwavelength, thickness and effective refractive index of meta-atom, respectively. The effective refractive index for a rectangular metaatom with a cross-section of $a \times b$ and the lattice constant of c is

$$n_{eff} = \frac{n_m(a \times b) + n_s\,(c^2 - a \times b)}{c^2}, \tag{2.2}$$

where n_m and n_s are the refractive indices of meta-atom and its surrounding medium. In this approach, the existence of Fabry–Pérot resonances can disturb the performance of meta-atoms in providing ϕ_{WG} as expressed in Eq. (2.1). So, to realize a metasurface with the propagation phase approach, it is necessary to implement electrodynamic simulations. It is worth mentioning that this method can also provide a polarization-sensitive metasurface [14]–[17].

2.1.2. Resonance phase

The early stage of phase gradient metasurfaces was initiated by resonance phases in plasmonic meta-atom [18]. Later, this technique was implemented in dielectric meta-structures which support different orders of electric and magnetic Mie resonances [19]–[21]. The interaction of the incident field with these resonance modes introduces phase discontinuities. For example, the phase of the incident field can jump π and $\pi/2$ after interaction with dipole and quadrupole modes, respectively.
The transmittance and the reflectance coefficients of the electric and magnetic Mie-type resonances can be written as

$$t = 1 + \frac{2i\gamma_{\mathrm{e}}\omega}{\omega_{\mathrm{e}}^2 - \omega^2 - 2i\gamma_{\mathrm{e}}\omega} + \frac{2i\gamma_{\mathrm{m}}\omega}{\omega_{\mathrm{m}}^2 - \omega^2 - 2i\gamma_{\mathrm{m}}\omega} \tag{2.3}$$

$$r = \frac{2i\gamma_{\mathrm{e}}\omega}{\omega_{\mathrm{e}}^2 - \omega^2 - 2i\gamma_{\mathrm{e}}\omega} - \frac{2i\gamma_{\mathrm{m}}\omega}{\omega_{\mathrm{m}}^2 - \omega^2 - 2i\gamma_{\mathrm{m}}\omega}, \tag{2.4}$$

where γ_{e} and γ_{m} are damping parameters of magnetic and electric resonances with the spectral position of ω_{e} and ω_{m}. By tuning the geometrical parameters of an individual meta-atom, these resonances can destructively overlap ($\omega_{\mathrm{e}}=\omega_{\mathrm{m}}$) with each other. In this case, if they have a similar spectral profile with an equal damping

factor, a zero backward scattering is accessible that facilitates the construction of an efficient metasurface. In the resonance phase method, the realization of 2π phase coverage can be achieved when a magnetic dipole resonance with π phase delay overlaps with an electric dipole resonance with another π phase delay [22].

2.1.3. Geometrical phase

Since the discovery of the geometrical phase by Pancharatnam in 1956 [23] and the generalization of that by Berry in 1984, the so-called Pancharatnam-Berry (PB) approach has become a prevalent method to analyze the propagation of waves. The PB phase describes the contribution of the polarization state of light in the phase modulation when it is twisted via a structure. To rotate the polarization state, light should travel through an anisotropic meta-atom where it experiences different refractive indices in the principal axes of the unit cell. When the meta-atom rotates with an angle of θ, an additional phase delay will be added to the propagated wave which is 2θ. To interpret the contribution of rotation angle in the phase modulation, the transformation matrix for a meta-atom with the rotation angle of θ can be written as

$$\begin{aligned}\hat{t}(\theta) &= \hat{R}(o-\theta)\begin{pmatrix} t_{\mathrm{u}} & 0 \\ 0 & t_{\mathrm{v}} \end{pmatrix}\hat{R}(\theta) \\ &= \begin{bmatrix} t_{\mathrm{u}}\cos^2\theta + t_{\mathrm{v}}\sin^2\theta & (t_{\mathrm{u}}-t_{\mathrm{v}})\sin\theta\cos\theta \\ (t_{\mathrm{u}}-t_{\mathrm{v}})\sin\theta\cos\theta & t_{\mathrm{u}}\sin^2\theta + t_{\mathrm{v}}\cos^2\theta \end{bmatrix}\end{aligned} \tag{2.5}$$

where $\hat{R}(\theta)$ is the rotation matrix and $\begin{bmatrix} t_u & 0 \\ 0 & t_u \end{bmatrix}$ is Jones matrix. Also, t_u and t_v refer to the complex coefficients of the transmitted field which are decoupled due to the anisotropic nature of meta-atom. Eq. (2.5) shows the component of the transmitted field when the meta-atom is excited by a right-handed circularly polarized wave. The transmitted field can be written as

$$\begin{aligned}\left(\mathrm{E}_i^{\mathrm{R/L}} = (\hat{e}_x \pm i\hat{e}_y)/\sqrt{2}\right) \\ \mathrm{E}_i^{R/L+} = \hat{t}(\theta)\cdot \mathrm{E}_i^{\frac{R}{L}} = \frac{t_u + t_v}{2}\mathrm{E}_i^{\frac{R}{L}} + \frac{t_u - t_v}{2}e^{\pm i2\theta}\mathrm{E}_i^{\frac{L}{R}}\end{aligned} \tag{2.6}$$

where R and L indicate the right and left-handed circularly polarized light. It can be seen from Eq. (2.6) that the transmitted light has two different types of handedness. The first term is related to unmodulated light with the same polarization and the second one refers to the cross-polarized component that experiences a PB phase shift of 2θ. For more details about the derivation of Eq. (2.6), see [24].

2.2. Materials and operating wavelengths

Development of metasurfaces started by utilizing plasmonic antennas as building blocks to provide full 2π phase coverage. Although the transmitted light can be artificially modulated by controlling the geometric parameters of plasmonic structures, they suffer from very large ohmic losses that limit their efficiency to around 10% [25]. So, the direction of development switched to rendering dielectric meta-atoms to improve the efficiency of the metasurfaces. Figure 2.1 illustrates some of the earliest works in plasmonic and dielectric metasurfaces.

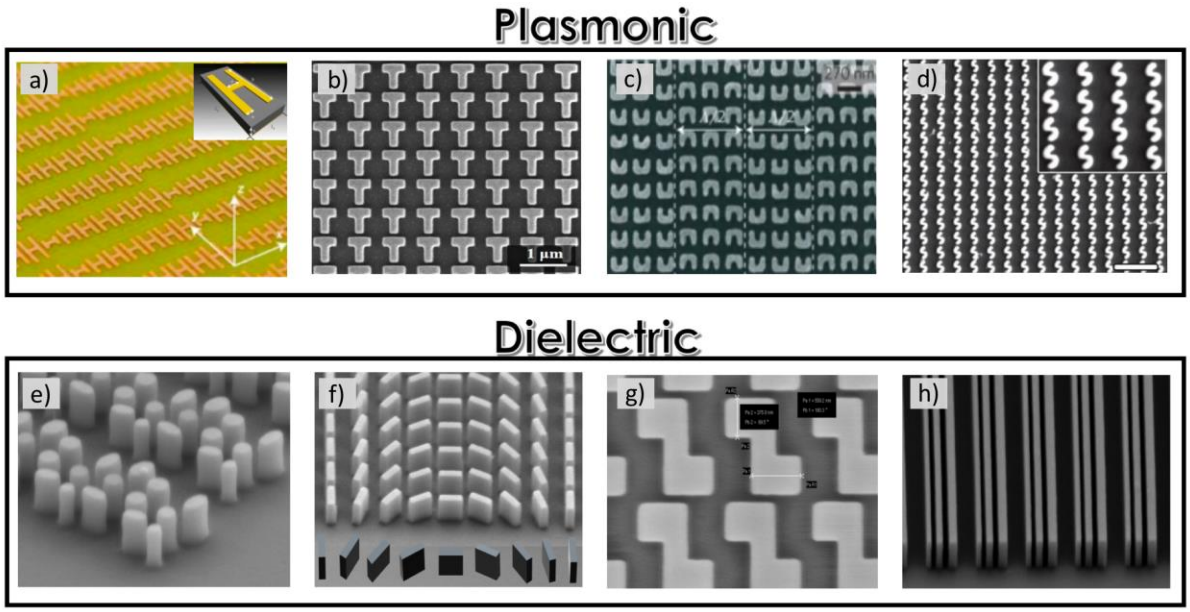

Figure 2.2: Different types of metasurfaces. Plasmonic structure in the top box and silicon-based metasurface as dielectric type in the second box. (a) H-shaped antenna array as a connection to link propagating waves to the surface waves [26]. *(b) T-shaped meta-atoms for polarization conversion* [27] *© 2012, Nature Materials. (c). U-shaped split-ring resonators with strong magnetic resonance* [28] *© 2015, Advance optical materials. (d) S-shaped metasurface to excite toroidal resonances* [29] *© 2021, Nature Photonics. (e-h) Fabricated silicon-based metasurfaces (Shanei, et al., unpublished data). (e) circular and elliptical metaatoms to bend the light, (f) nano-fins as a phase gradient beam deflector patterned by geometrical phase approach, (g) chiral structure by periodic z-shaped meta-atoms and (h) elongated bars as meta-grating.*

To support extensive phase coverage required for beam shaping and highly efficient devices, the constitutive materials used for dielectric metasurfaces need to have a high refractive index (n) and low extinction coefficient (k). Typical materials used for dielectric metasurfaces are shown in Fig. 2.3, considering their refractive indices and operating wavelengths. Commonly used materials such as Si, GaN, GaAs, TiO_2 are briefly explained in the following parts.

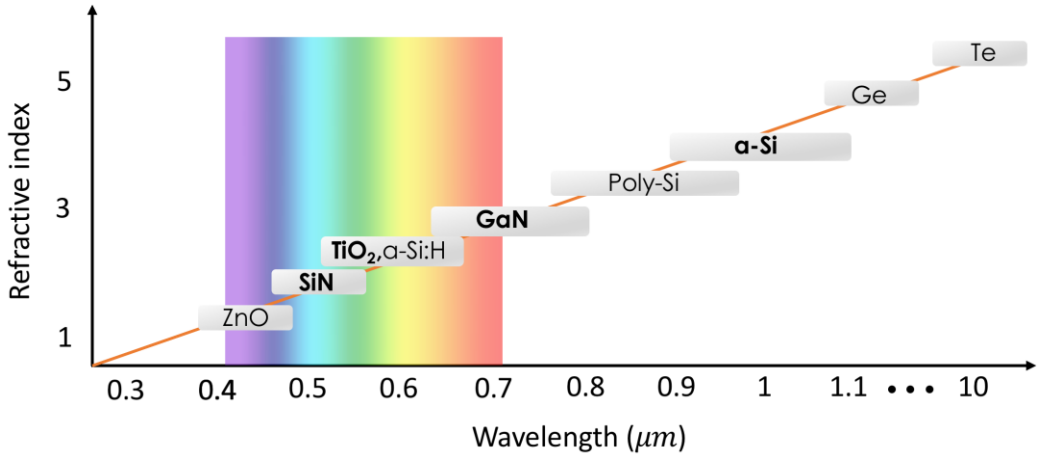

Figure 2.3: High-index dielectric materials used for metasurfaces. Silicon-based meta-atoms are a useful option for IR and near-IR regimes that can exhibit high efficiency in lower aspect ratios because of their high refractive indices. These kinds of metasurfaces can also be implemented as Huygens' metasurfaces with a low aspect ratio [3], [30]–[32]. *TiO_2-based metasurface with lower refractive index (at visible) in comparison to silicon (at infrared) usually consists of truncated waveguides resonators with propagating modes* [33]–[35]. *GaN and GaAs meta-atoms with a favorable refractive index can generally present highly efficient metasurface at visible and near-IR. SiN-based metasurfaces have almost lower efficiency than other dielectric metasurfaces, which can be used in long wavelengths of visible light* [36], [37].

Si-based metasurfaces
Fabrication of Si metasurfaces is compatible with CMOS technology and, later, a suitable material for integrating with other silicon-based optical devices. Due to the low dispersion of silicon meta-atom at near-infrared frequencies, they are good candidates as a constitutional element for highly efficient metasurface [3], [30]–[32].

TiO_2-based metasurfaces
TiO_2 is optically transparent at visible ranges with a small extinction coefficient (k), making it the best candidate to use in most metasurfaces, which work at green to red wavelengths [38]. Since this material is chemically more stable than silicon, a hard mask should be used in the fabrication process of TiO_2 metasurfaces that add complexities to its fabrication process [39]–[43]. The Capasso group was a pioneer in introducing and developing TiO_2-based metasurfaces as multi-color metalenses [33], [34].

GaN and GaAs-based Metasurfaces
GaN and GaAs can be suitable replacements for TiO_2 metasurfaces when the fabrication complexity determines the material and type of metasurfaces. The fabrication process of this material is compatible with LED and laser technologies and can be a low-cost option for metasurfaces. These materials also have much lower losses at visible ranges than their silicon counterparts [44], [45]. The Tsai group was one of the first groups that proposed this kind of metasurface [46]. These metasurfaces are suitable for integration with other photonics devices, such as vertical-cavity surface-emitting lasers (VCSELs) [47].

SiN-based Metasurfaces
The SiN_x with a band gap of 2 eV is a good candidate for the building block of metasurfaces when the thermal stability and some mechanical properties are important for the target application [36], [37]. This material is less transparent in comparison with TiO_2 and GaN materials. The Atwater group suggests SiN metasurfaces for the space application of metasurfaces [48].

2.3. Design methodologies and configurations

In the current literature, methods to find a suitable building block for a metasurface are divided into two techniques: forward and inverse designs. Usually, forward or conventional techniques implement full-wave numerical analysis with topological parameter sweeps and optimization algorithms. However, this technique is usually useful for meta-devices with applications such as focusing (metalens) or bending (meta-deflector). It is time-consuming if the aim is to design a multifunctional, broadband, or tunable metasurface. Therefore, developing an accurate, fast, and efficient approach that finds a proper building block to enable a versatile metasurface is essential. Inverse design can be an excellent method to tackle the drawbacks of conventional forward techniques where the optical response of the metasurface serves as input and the structural geometry and feature sizes are the outputs [49]–[52]. Figure 2.4 summarizes the required steps for the forward design method.

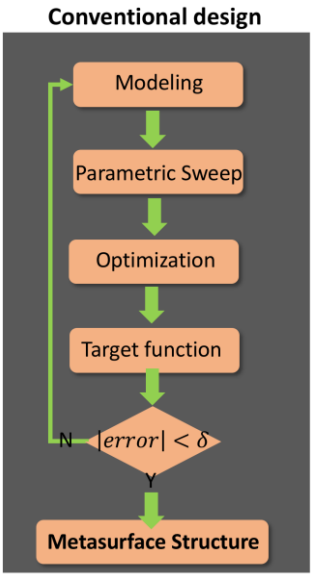

Figure 2.4: Forward technique to design the building block of the metasurface by using topological optimization data [49].

The next step after obtaining a library of proper meta-atoms is their arrangement on a surface. Usually, the configuration of metasurfaces is determined by the function of required phase and/or amplitude profiles. A straightforward method to decorate a metasurface is discretizing a surface based on the meta-atom lattice constant and then distributing the building block over the surface to generate the required phase and/or amplitude masks. Although this method works properly for static, single wavelength/function meta-devices, there is a demand for adding other degrees of freedom to have multi-wavelength/functions and tunable platforms. Figure 2.5 illustrates some techniques that are used to enhance the functionality of the metasurface, such as dividing the surface into different areas [53], interleaving meta-atoms [54], [55], and using multi-layer [56] or reconfigurable metasurfaces [57].

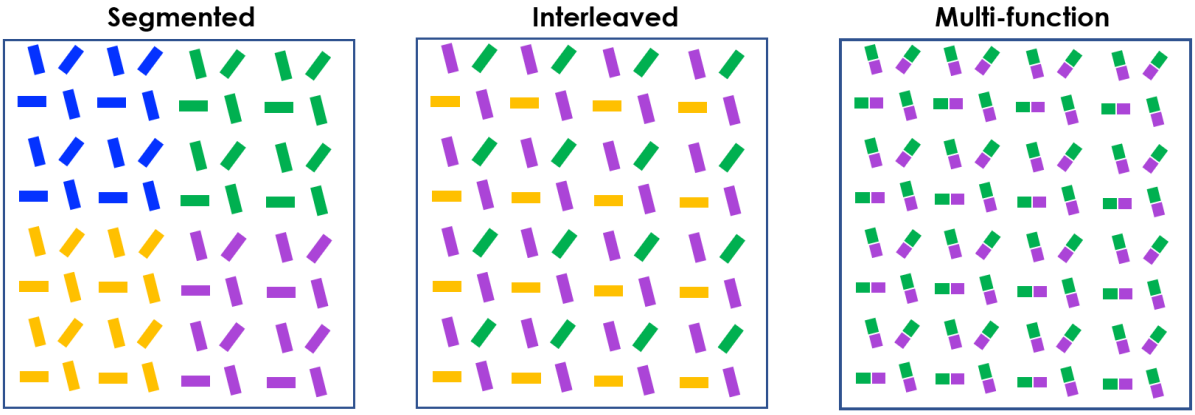

Figure 2.5: Examples of configuration techniques to enhance the functionality of metasurfaces by dividing metasurface into different segments (left box), multiplexing meta-atoms into a unit cell (middle box) and multi-function meta-atoms (right box).

2.4. Passive and active metasurfaces

While a passive metasurface generally presents a single function, an active type enables dynamic modifications of functions and performances based on the different actuation mechanisms. For example, Figure 2.6 shows various adaptive devices such as passive, switchable, and tunable metalenses.

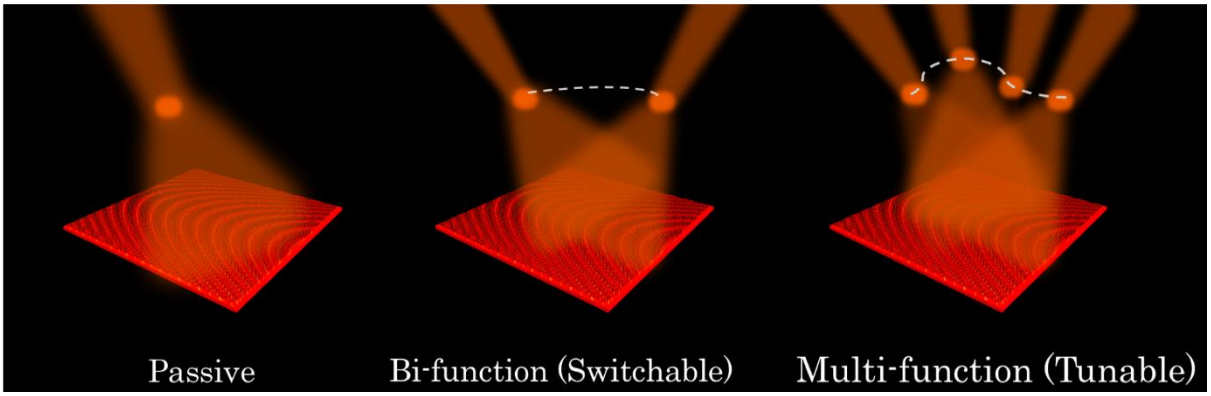

Figure 2.6: Examples of a passive meta-device on the left and two adaptive devices of switchable and tunable metasurface on the right side.

The potential of metasurfaces in the active tuning of performance makes them a versatile platform compared with conventional bulky systems. During the past decade, significant parts of research in metasurfaces have been dedicated to the development of active devices. Figure 2.7 shows statistics of the total number of papers for passive and active metasurfaces.

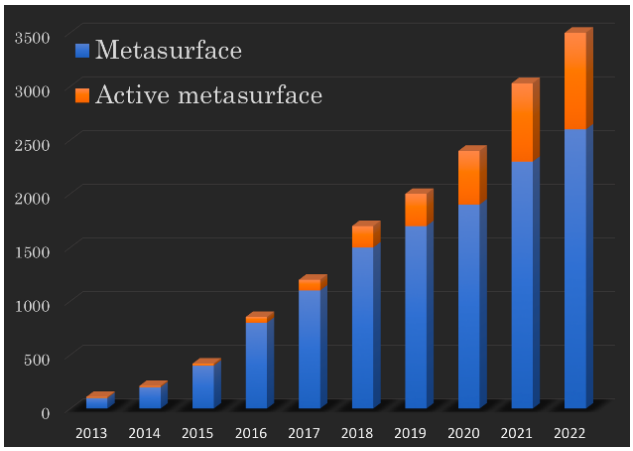

Figure 2.7: Comparison between the development of metasurface and its active types through the number of published papers extracted from the web of science (WOS) from 2013 to 2022.

To convert a passive metasurface into an active one, different methods can be implemented to design a metasurface, such as reconfiguring or rearranging the meta-atoms or changing the surrounding environment of meta-structure or using active phase-change materials (PCM). PCM based-metasurfaces are the most prevalent example of the active metasurface, which is related to implementing a tunable material such as liquid crystal, 2D materials, and semiconductors as an additional layer or building block of the metasurface. An external excitation can modulate the properties of these materials via electrical, optical, or thermal field. Table 2.1 summarizes some of the articles in the literature on active metasurface based on tuning mechanism, speed, efficiency, working wavelength, and phase coverage.

Method	Phase shift	Working wavelength	Efficiency	Speed range	Function	Drawbacks
Electrical tuning based on conducting oxide	300	NIR	<30%	GHz	Beam deflector Lens	Low efficiency Reflection mode
Electrical tuning base on 2D material	240	NIR	50%	GHz	Lens Absorber	Limited wavelength
Electrical tuning based on LC	360	Visible to NIR	36%	KHz	Color filtering SLM	Slow switching
Phase change material	70	Visible to NIR	75%	KHz	Bifocal lens Holography	Slow switching Non compatible
Mechanical Reconfigurable	300	Visible to THz	90%	MHz	Filters Lens	Difficult actuation installation
Flexible metasurface	360	Visible to NIR	90%	-	Color filter Lens	Sensitive Low speed
Nonlinear effect	360	NIR	<10%	Hz	Optical switch Frequency conversion	Low efficiency
Transition metal	90	Visible to NIR	35%	Hz	Holography Beam bending	Slow speed
Microfluidic based	-	Visible to NIR	55-70%	Hz	Color display	Low efficiency

Table 1 Review of recent papers in active metasurface based on tuning mechanism, phase coverage, working wavelength, efficiency, modulation speed, target function and limitations [55]–[63].

Lastly, let us note that a chiral structure can selectively respond to light due to its polarization-dependent behavior. Chiral metasurfaces consist of inherently passive meta-atoms which take the polarization state of light as a tuning knob to demonstrate a tunable performance. Figure 2.8 shows a chiral silicon metasurface that acts as a reflector and transmitter for right and left-handed circularly polarized light, respectively.

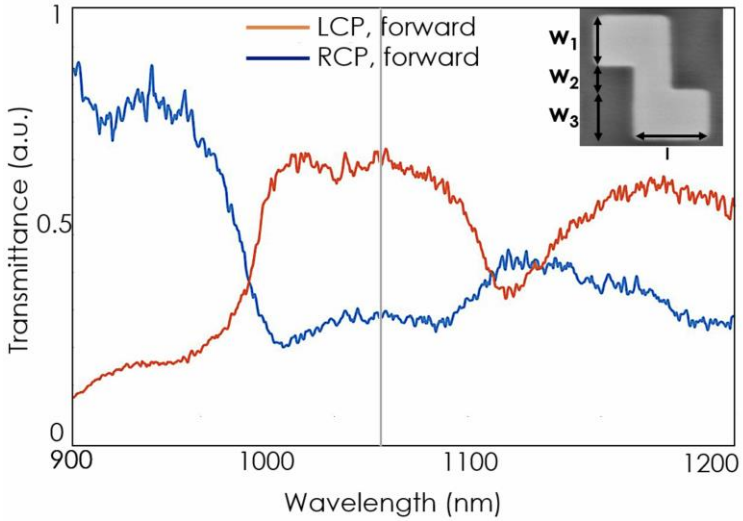

Figure 2.8: FDTD simulation results of transmission spectra of periodic z-shaped meta-atoms. At 1064 nm, the meta-atom can actively transmit or reflect by switching the incident polarization. SEM image of fabricated subwavelength silicon meta-atom is shown in the inset with a thickness of $500\ nm$*, periodicity* $800\ nm$ *of* w_1 *and* $w_3 = 260\ nm$*,* $w_2 = 150\ nm$ *and* $l = 500\ nm$ *(Shanei, et al., unpublished data).*

2.5. Applications and research frontier

After developing fundamental queries in metasurfaces, researchers mostly focused on the basic applications such as focusing, bending, or other kinds of beam shaping, as illustrated in Fig. 2.9. Beam sculpting with phase gradient metasurface is the basis of different applications, such as imaging, spectroscopy, bioscience, and particle manipulation. Optical manipulation of micro-scale objects is the main subject of this thesis.
In 2019, compact meta-devices were acknowledged as one of the top 10 emerging technologies [58]. Since the main focus of this thesis is utilizing the optical forces and torques arising from a focused and bent light, the

following two sections are dedicated to investigating the required phase profiles for the metalens and meta-deflectors.
Research within metasurfaces is developing very fast due to their use in many applications in different fields of science and, even more recently, in some industrial technologies, such as replacing multiple optical elements in existing ST ToF modules with flat metalenses.
.

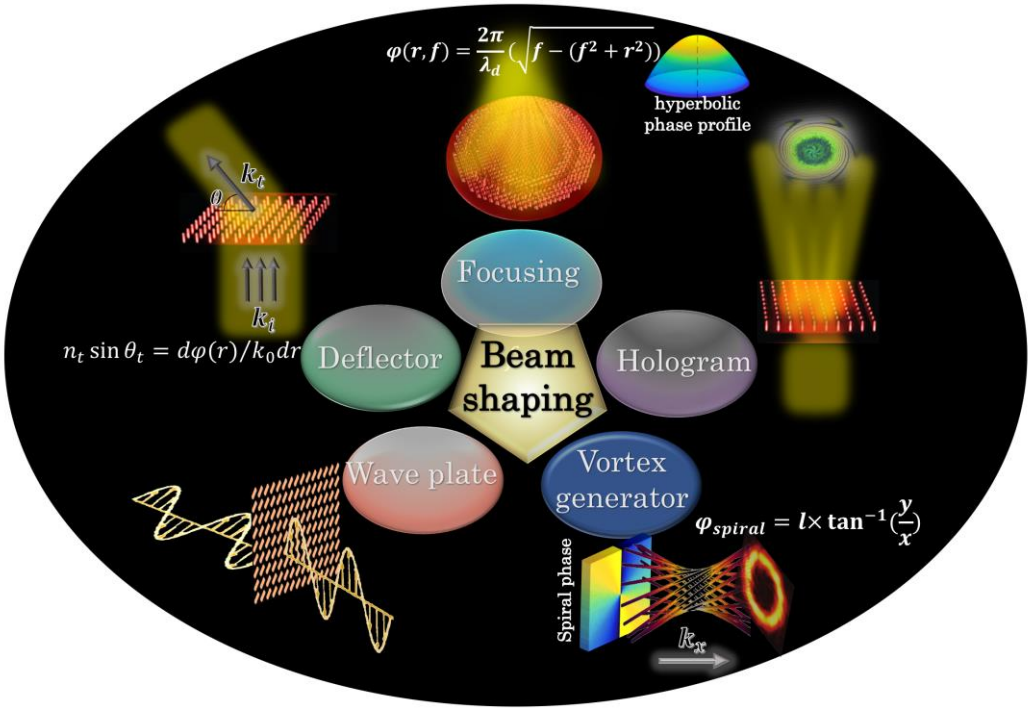

Figure 2.9: Illustration of different applications of optical metasurfaces in wavefront shaping. Top: Spherical metalens with hyperbolic phase profile of $\varphi(r,f)$ construct a hot spot with a focal length of f by patterning meta-atoms in two-dimension. Left: Meta-deflector bends a normally incident beam at an angle of θ_t in a medium with a refractive index of n_t by distributing meta-atom based on the phase profile of $\varphi(r)$. Right: Holographic circular ring achieved by defining a phase mask derived from computer-generated holography calculations. Bottom left: Half-wave plate patterned by a periodic array of meta-atom oriented at 45° converting the input into an output beam whose polarization is orthogonal to the incident polarization. Bottom right: Vortex beam generator achieved by implementing a spiral phase profile of $\varphi(x,y)$ proportional to the topological charge of l.

2.5.1. Beam focusing with metasurfaces

The phase modulation of a metasurface must cover a full 2π range to shape an incident wavefront efficiently into any arbitrary profile. As discussed in section 2.3.3, different approaches such as PB, resonance and propagation phase have been used to control the extracted phases from metasurfaces.
Optical trapping using metalenses is a prevalent example of using a planar structure for the compact manipulation of particles. In recent years, various demonstrations have been presented by different groups [10] where the phase profile of Eq. (2.7) is used to focus a plane wave and can be written as

$$\varphi(r_0) = -\frac{2\pi}{\lambda}\left(\sqrt{r_0^2+f^2}-f\right). \tag{2.7}$$

Here f, λ and r_0 are the focal length, operating wavelength and radial coordinate, respectively. If the x and y-coordinate contribute to the radial position of r_0, the structure constructs a spherical lens with a single focal

spot. When the arrangement of meta-atoms is based on one coordinate in Eq. (2.7), the scattered waves interfere constructively at a focal line.

2.5.2. Beam bending with metasurfaces

The advent of metasurfaces started with the generalization of Snell's law in 2011, where an in-plane phase gradient of $\frac{d\varphi}{dy}$ is considered at the interface of two media with the refractive indices n_t and n_i in y-direction. In this case, by considering Fermat's principle, the variation of the phase gradient can be written as

$$n_t sin(\theta_t) - n_i sin(\theta_i) = \frac{1}{k_0}\frac{d\varphi}{dy}. \tag{2.8}$$

Here, by considering the first and second terms in Eq. 2.8 as the wavevectors of the incident and transmitted beam in the y-direction, the generalized Snell's law can be simplified into

$$\Delta k = k_o - k_i = \frac{d\varphi}{dy}\hat{y}, \tag{2.9}$$

which reveals the dependency of the wavevector's variation to the phase gradient at the interface.

Chapter 3

Manipulation of micro and nano-objects

Mechanical manipulation of objects like trapping, positioning, and sorting has attracted interest in recent years due to its promising potential in different fields of science, such as drug delivery, sensing, and diagnostics [59]. Figure 3.1 shows the number of publications on manipulating and controlling micro-scale objects using the terms micro-swimmer or microrobot. It is worth mentioning that in the current literature, micro and nano-objects have been referred into different terms such as a robot, motor, rotor, swimmer, vehicle, etc.
The mechanisms used to control particles are divided into two main categories of exogenous actuations, such as magnetic, acoustic, and optical fields, and endogenous actuations, such as biohybrid and chemical energy sources [58], [59]. A brief review of different actuation mechanisms is presented in the first part of this Chapter. Then, various types of optical forces and torques are described to reveal the nature of light-matter interaction by focusing on momentum exchange between light and target objects.

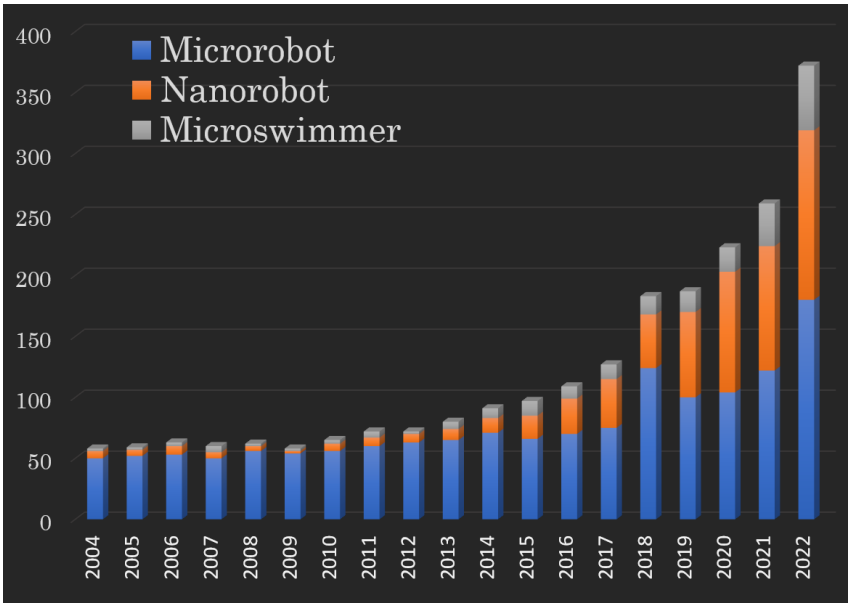

Figure 3.1: Number of publications containing the terms microrobot, nanorobot and micro-swimmer. The data is extracted from the web of science (WOS) from 2004 to 2022.

3.1. Field-driven manipulation of micro-objects

The essential part of manipulating a particle is the actuation energy source that controls the performance of the manipulation mechanism. Although self-driven micro-objects can receive their required triggering energy from the environment, an external source is often required to provide a user-controlled or automated manipulation of objects [57]. The spatial position of an object can be manipulated by various energy sources, including bio-hybrid actuation, electrical field, acoustic wave, light radiation, and magnetic field, depending on the material and its surrounding environment. In addition, to govern an accurate, stable and flexible actuation, multi-source excitations have been utilized for more degrees of freedom. Figure 3.2 shows various types of particle manipulations based on actuation mechanisms.

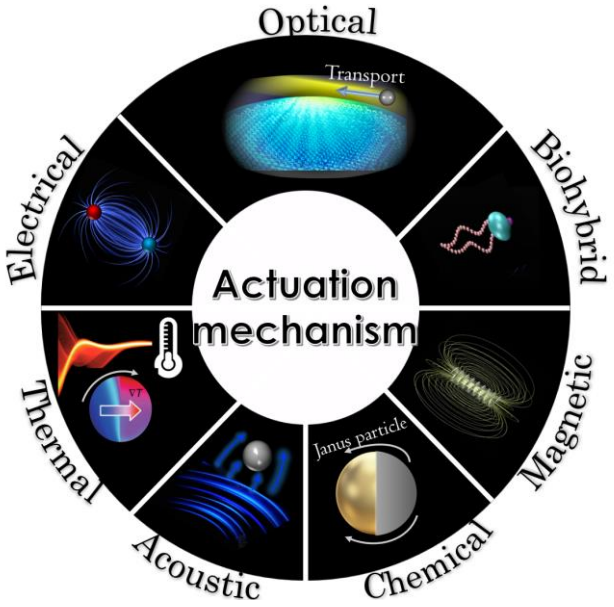

Figure 3.2: Different types of actuation mechanisms to manipulate micro and nano-objects.

- **Biohybrid sources** are the most biocompatible energy source activated by the conjugation of living entities as cargo to the target objects [60], [61]. However, while this source is suitable for swarm control of objects, its application is limited due to the low accuracy and poor controllability [62]. The first example of manipulating micro-scale objects by rod-shaped bacteria as a biohybrid power source was demonstrated by Darnton et al. [63]. Additionally, biocompatible enzymes can be implemented as a carriage to transport objects at the nanoscale [64].
- **Magnetic field** is a useful actuator for medical applications that can easily penetrate the tissue. This kind of actuator provides the possibilities for transporting, tumbling, spinning, and morphing the shape of a magnetic structure. However, using magnetic field as a driving force presents some practical challenges, such as complex large hardware equipment, difficulties in film coating and other treatments of the substrate, particularly nano-scale manipulation [65]–[69].
- **Chemical actuators** are a popular research area extensively studied to control single or even swarms of micro-objects. This type of actuation may overlap with biohybrid mechanisms where living entities are used to activate a chemical reaction [70], [71]. In one of the first experiments of chemically driven particles, high concentrations of toxic hydrogen peroxide were used to activate a series of reactions [72]. In recent years, better bio-compatible candidates were introduced, such as water conversion reactions and biofluids [70], [73].
- Other types of sources such as **electrical** [74]–[76], **thermal** [77], [78] and **acoustic fields** [79], [80] are less applicable in comparison with the other introduced actuators due to low accuracy, resolution and depth of penetration.

Lastly, light is an important energy source with different degrees of control for particle manipulation. Light can provide rapid, precise and tunable possibilities for real-time manipulation of an object. This report focuses on exploring light-driven transport of micro-objects, which is investigated in detail in the following sections.

3.2. Light-driven manipulation of microparticles

In the past two decades, optical manipulation has advanced significantly, finding use in various research fields, such as condensed matter physics, chemical physics and biological science. Optical manipulation enables precise and flexible manipulation of micro-objects, rendering itself remarkable attention from the bioscience community [81]–[84].
Light-powered microrobots are divided into indirect and direct groups according to the driving mechanisms. For indirect optical manipulation, light acts as a primary source that activates a secondary mechanism, which facilitates the control over the microrobot. For direct optical manipulation, microrobot actuation arises exclusively from energy and momentum exchange in light-matter interaction, without any secondary phenomenon. The following section aims to introduce these types of light-assisted manipulation of objects.

3.2.1. Light-assisted indirect optical manipulation

Photochemical manipulations

Photochemical actuators convert optical energy into kinetic energy through chemical reactions. These reactions are initiated by the absorption of optical waves using two main mechanisms: photochromic and photocatalytic effects. For example, Janus particles and elongated structures, such as rod-shaped particles can be manipulated using this method. To control these objects, an unbalanced gradient on opposite sides of the structure is required. This gradient can either arise from the different composition of materials or uneven reactions inside the core and surrounding body. Figure 3.3 illustrates a schematic of these micromotors with rotation, translation, aggregation and rolling motions [85], [86].

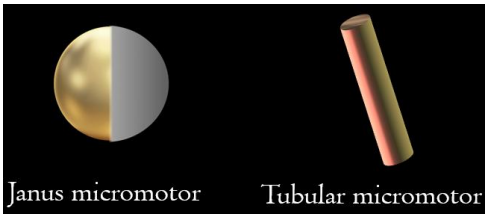

Figure 3.3: Two examples of microrobots using photochemical as a driving actuation mechanism.

Photothermal manipulations

Photothermal manipulation relies on absorbing materials to convert optical energy into a thermal distribution around the target object [87], [88]. The diffused heat usually decays in the outward direction, forming a gradual temperature gradient that provides the required energy for propulsion. On the other hand, it is also possible to accumulate particles by thermocapillary flows that stream toward the structures. Another example of photothermal manipulation is based on constructing an intermediary agent, such as a bubble at the interface, to transport objects [88], [89]. In this technique, a programmable and tunable temperature gradient can be induced by engineering the spatial positions of lossy structures and using birefringence elements, respectively.

Photomechanical manipulations

Photomechanical actuation mechanisms depend on the interactions between light and/or mechanically photo-responsive materials such as liquid crystals [90], [91], hydrogels [92] and shape memory polymers [93]. The structural shape of these materials relies on the alignment of the molecular phases. For example, a liquid crystal can switch the orientation of its molecular phase from order to disorder when excited by an external optical field. This transition can modify the spacing between the molecules, which forms a mechanical motion for soft material. More details have been reviewed in [94].

Optoelectronic manipulations

Optoelectronic-based tweezers are the most tunable and user-friendly approach among the introduced optically assisted manipulation. This technique was invented in 2005 by Chiou and his group [95]. Then, it attracted attention due to its high efficiency and reliable manipulation of objects. Usually, the required structured light in this system is a LED equipped with a digital micromirror device (DMD). The impinging light can locally modulate the impedance of a photoconductive substrate, such as hydrogenated amorphous silicon, to induce a varying electric field over the surface. This non-uniform field generates dielectrophoresis (DEP) forces in the scale of nano-newtons which control the position of the target object even with a size larger than 100 micrometers [96]. Various examples of the technique have been studied in the recently published papers of [97], [98].

3.2.2. Direct optical manipulation

As early as 1619, Kepler described that the deflection of the comet's tails could be due to the interaction of dust with sunlight. Two centuries later, Maxwell's theory demonstrated the propagation of electromagnetic pressure can be applied to an object. In 1905 Einstein used Plank's theory to explain the photoelectric effect. He introduced photons as quanta of energy of light, which can carry a well-defined momentum. Then, Compton experimentally showed the momentum exchange between X-ray photons and electrons in 1925. A few years later, Frisch successfully transferred the momentum of the photons to an atom [99]. The revolution and fundamental studies of momentum exchange between light and matter continued till 50 years ago when Ashkin did a series of studies in the optical trapping of a dielectric particle with a focused laser light [4]. They demonstrated that a three-dimensional stable optical trapping can be achieved by a tightly focused laser light for various shapes and materials, including dielectric and metallic micro-objects. This kind of direct confinement and manipulation of particles is known as optical tweezers. Due to the various degrees of freedom of optical tweezers, it is not surprising that they can also be widely used to control objects at the micro and nanoscale. The prerequisite for developing optical tweezers relies on the advances in the progress of optical forces and torques [100].

3.2.2.1. Optical forces

While early studies of optical trapping and manipulation of matter were based on the radiation pressure of light, which is in its propagation direction, optical confinement of particles relies on the optical force that originates in the spatially inhomogeneous intensity profile. In this section, these types of optical forces are introduced to describe the basic working mechanisms of an optical tweezer.

To explain how an optical tweezer can manipulate a particle, Fig 3.4 (a) shows a Gaussian light with two beam rays transmitted through a particle located off-axis of the beam. As shown with arrows, the scattered rays propagate at different angles because of the refraction of the light rays. Hence, the scattered light acquires different momentum than the incident light. Based on the conservation law of momentum, the driving force (F_a) should be exerted on the particle toward the higher intensities on the right side to compensate for the changes of momentum during the scattering process. The other ray can also exert an optical force (F_b) on the particle. Due to the Gaussian distribution of the incident beam, the optical force F_a is stronger than F_b, which moves the particle toward the center of the beam. The same thing can happen when the particle's initial position is at the right side of the center of the maximum intensity of the beam. In addition, the scattered rays push the particles along the direction of propagation of the light beam, as shown in Fig. 3.4 (b).

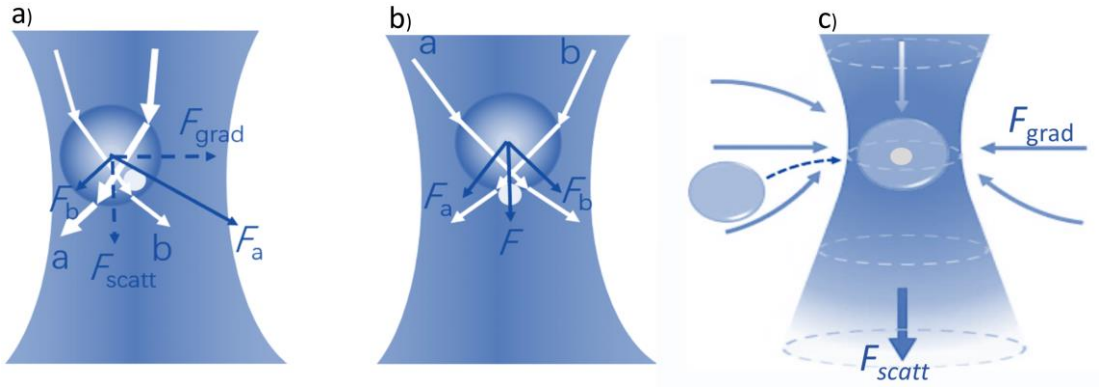

Figure 3.4: Schematic illustration of conventional optical tweezers for three-dimension confinement of a particle(a) Particle is located away from the focal point or center of a Gaussian beam and moved toward higher intensities at the center. (b) Particle is pushed to the center of the focal point, and (c) 3D-confinement of a particle at the center of a tightly focused beam.

The optical forces in a focused light beam can be divided into absorption, scattering and gradient forces. The scattering and absorption forces are common optical forces that can be observed when an incident plane wave impinges on an obstacle. The gradient force appears due to the non-uniform distribution of the light beam, as shown in Fig 3.4 (c) [4], [101]. For example, this varying profile can be observed in a tightly focused beam.
The scattering force pushes the object in the axial direction parallel to the beam propagation while the gradient force arising from the potential well created by the non-uniform intensity distribution tends to confine the particle close to the focal region. If the gradient force is enough to overcome the scattering force, a three-dimensional optical trap is achieved. For a modestly focused beam, a particle can be trapped in the transverse plane from the intensity gradient force, and in the propagation direction by using an interface, against which the particle is being pushed by the scattering force. For example, two-dimensional manipulation can be useful to trap absorptive plasmonic nanoparticles.
A quasi-static calculation can be employed through the Lorentz force to calculate the optical force acting on a small spherical particle in the Rayleigh regime. When the induced dipole moment in the particle has a linear dependency on the monochromatic incident electric field [102], [103], the induced dipole moment can be defined as $p(\mathbf{r}) = \alpha(\omega)\mathrm{E}(\mathbf{r}_0)$ with polarizability of α related to the electric field at the r. Then, the time-averaged force can be written as

$$\langle \mathbf{F} \rangle = \frac{\alpha'}{2} \sum_i \mathrm{Re}\{\mathrm{E}_i^* \nabla \mathrm{E}_i\} + \frac{\alpha''}{2} \sum_i \mathrm{Im}\{\mathrm{E}_i^* \nabla \mathrm{E}_i\}, \tag{3.5}$$

where * is the complex conjugate sign. The first term is related to the inhomogeneous electric field and the real part of the polarizability. The second term is associated with a non-conservative force proportional to the imaginary part of polarizability, see [102], [103] for more details. It was shown that by substituting the complex amplitude of the electric field with the real amplitude of E_0, the expression in Eq. (3.5) can be simplified to

$$\langle \mathbf{F} \rangle = \frac{\alpha'}{4} \nabla E_0^2 + \frac{\alpha''}{2} E_0^2 \nabla \Phi, \tag{3.6}$$

where $\Phi(\boldsymbol{r})$ is the phase of the electric field. This equation reveals that the variation of the phase gradient inside the electric field can also generate optical forces. In this case, the phase gradient can redirect the scattering force along the axial direction to the transverse plane. This redirected component adds a complementary knob in the optical manipulation of the particles. In 2008, the first group demonstrated theoretical and experimental proof that optical forces can arise from the phase gradients, see [104].

Optical torques

Photons in an elliptically polarized light can carry intrinsic linear and spin angular momenta. The linear momentum, $\hbar k = \hbar\omega/c$, depends on the frequency of light, and the spin angular momentum (SAM) equivalent to $\pm\hbar$ is independent of frequency. The third non-intrinsic momentum that a beam can carry is orbital angular momentum (OAM), which is related to the spatial distribution of a beam. For example, a Laguerre–Gaussian beam carries OAM given by $\ell\hbar$ per photon where ℓ can be any integer [105], [106].

Each of these momenta can drive the object in a different trajectory. While the linear momentum of the light can translate the object, the rotational movement is related to the exchanges of angular momentum between light and object. The mechanical observation of light-induced optical torques by leveraging an angular momentum of a beam was first demonstrated experimentally by Beth et al. [95]. Later, researchers separately investigated mechanical motion induced by SAM or OAM. The SAM can rotate the object around its axes based on the polarization of the incident beam. The OAM provides orbital rotation around the axes of the impinging light, such as Laguerre–Gaussian beams [96]–[99]. Figure 3.4 shows a schematic of the spinning and orbiting of a particle for a circularly polarized and helical beam on the left and right sides.

To calculate the mechanical rotation of an object around its axis driven by an external optical torque of M_e, the variation of angular velocity can be written as [107]

$$\frac{d\omega}{dt} = (M_f + M_e)/J, \tag{3.10}$$

where M_f is the viscous frictional torque counteracting in the opposite direction of the angular velocity and J is the moment of inertia proportion to the radius squared and the object's mass.

A general approach to calculating the angular momentum for a small spherical particle is using the time average of optical torques in the perpendicular plane to the propagation direction of the incident field E [108]. By using the dipole approximation, the optical torque can be written as

$$\tau = \langle p \times E \rangle, \tag{3.11}$$

where p is the electric dipole strength.

The optical torque can be split into two components of absorption and scattering. The absorption part can be estimated directly through the object's absorption cross-section and the incident light's intensity. For the case of an isotropic object and circularly polarized light of $\mathbf{E} = \frac{E_0}{\sqrt{2}}(\hat{x}\cos\ \omega t + \hat{y}\sin\ \omega t)$, the external optical torque of M_e exerted on the particle is mainly because of the absorption of SAM of the electric field, which can be written as

$$M_e = \hat{z}\frac{n_m^2}{2}\mathrm{Im}\{\alpha\}|E_0|^2. \tag{3.12}$$

For a birefringent particle, the optical torque can be transferred to the particle due to the scattering and also the absorption of the incident light ($M_e = M_{scat} + M_{abs}$). For a more complicated system, the M_e can numerically be calculated from Maxwell's stress tensor from the electrical field distribution.

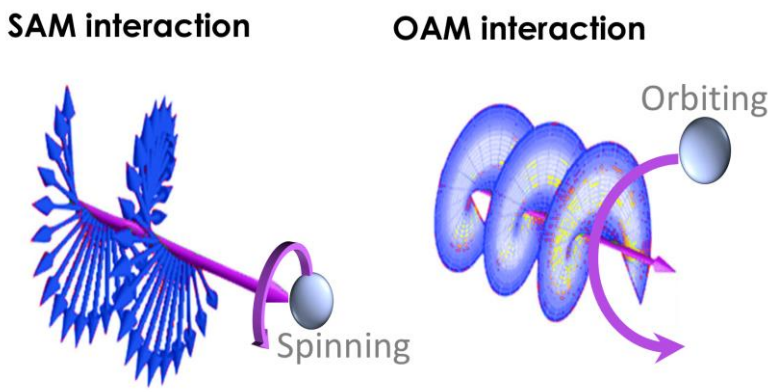

Figure 3.5: Schematic illustration of the spinning and orbiting of a particle through the polarization state of the light (SAM) and a structured vortex beam (OAM), respectively.

Chapter 4

Optical manipulation with meta-structures

Metasurfaces with engineered subwavelength building blocks can provide two possibilities for shaping the scattered wavefront. The first approach is shaping the wavefront by a large-scale stationary metasurface before the object. In this case, metasurfaces can be a compact replacement for conventional bulky optical elements, such as lenses and spatial light modulators (SLMs), used to modulate light. The second technique to manipulate the momentum exchange between light and matter is incorporating a metasurface into a micro-scale object [109],[111]. So, the metasurfaces are subjected to momentum exchanges which are also caused by themselves. Figure 4.1 illustrates some examples of various degrees of freedom that a metasurface can provide to engineer the optical force and torque.

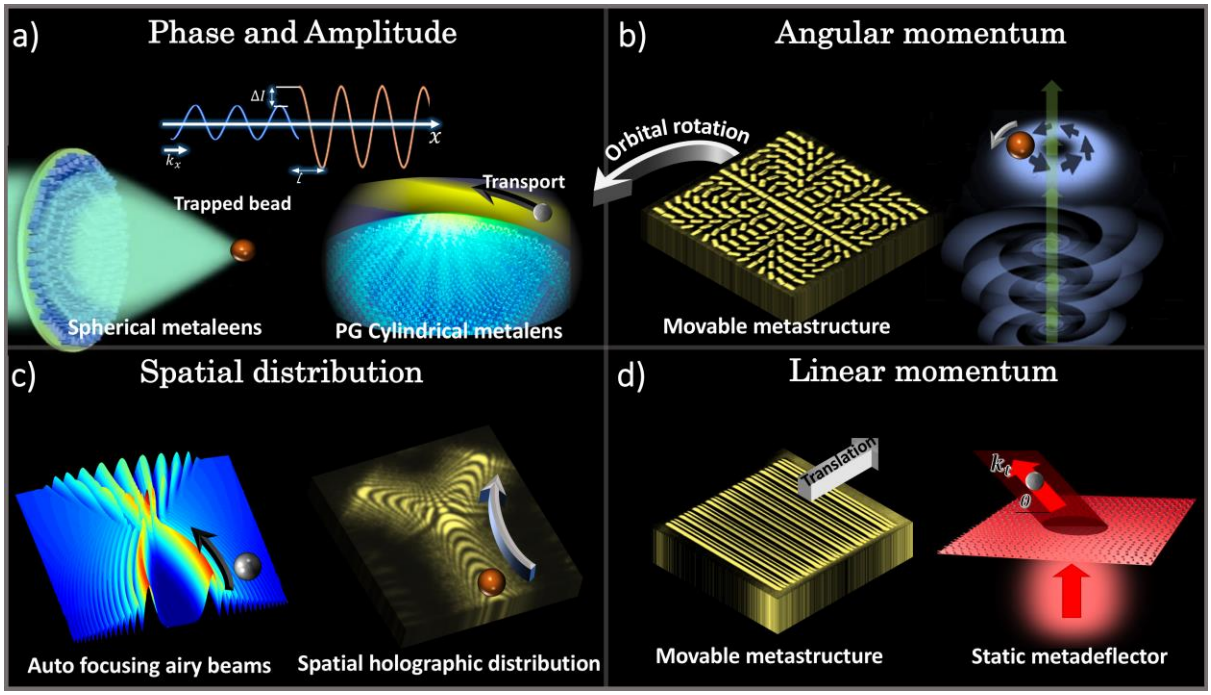

Figure 4.1: Illustration of the optical manipulation with metasurfaces based on different degrees of freedom of light beam. a: Spherical metalens that provides three-dimension confinement of particle (left side). Cylindrical with a phase gradient along its focal line to confine and transport the particles (right side). b: Free meta-particles with the embedded metasurface can orbit around the optical axis of the propagated helical beam (left side). A vortex beam from a static metasurface can orbit the beads in the bright area (right side). c: Particle transport by two symmetric airy beams and confinement in the focal area constructed by the constructive interferences of two beams (left side). Particle transport in a Y-shaped holographic pattern with a phase gradient inside branches (right side). d: Movable free meta-particle translates in the opposite direction of the deflection of the light by the embedded gratings inside the body of the particle (left side). Static metasurface that can move the particle by the radiation pressure in the illustrated direction (right side).

4.1. Phase and amplitude modulations

Two examples of trapping with the cylindrical and spherical metalens are shown in Fig. 4.2 for two and three-dimension trapping, respectively. These metalenses are defined by a PB phase approach that has been used to realize the target phase of Eq. 2.1 with a-silicon meta-atom with a refractive index of 3.8 located on the top of the glass.

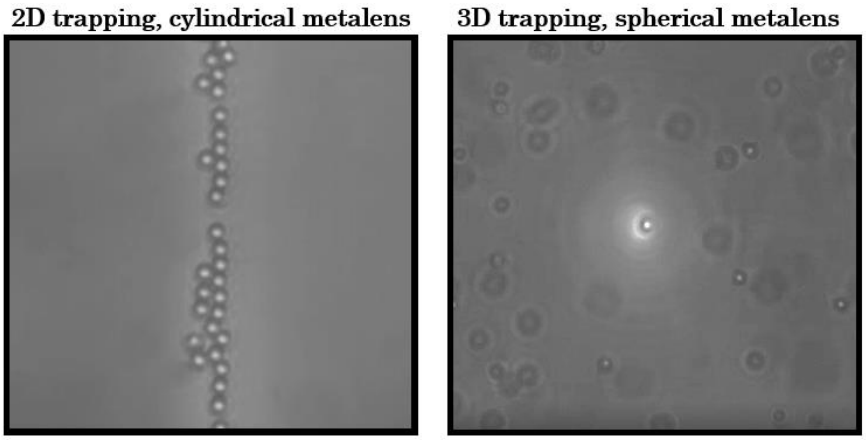

Figure 4.2: Two and three-dimension trapping using cylindrical and spherical metalens in the left and right boxes (Shanei, Engay, et al.). The metasurfaces were excited by a left-handed circularly polarized light at 1064 nm with the intensity of 5.5 and 3 $\mu W{\cdot}\mu m^{-2}$ for the cylindrical and spherical lenses, respectively.

In cylindrical metalens phase profile, adding a phase profile, such as in $\varphi(y)$ from Eq. 2.8, can directly print a linear phase gradient along the focal line in the y-direction. This term can re-direct the scattering force from the axial direction into the transverse plane, causing phase-dependent optical forces. This type of optical force can transport the trapped particles, as discussed in detail in the supplemented paper and shown in the snapshots of Fig. 4.3.

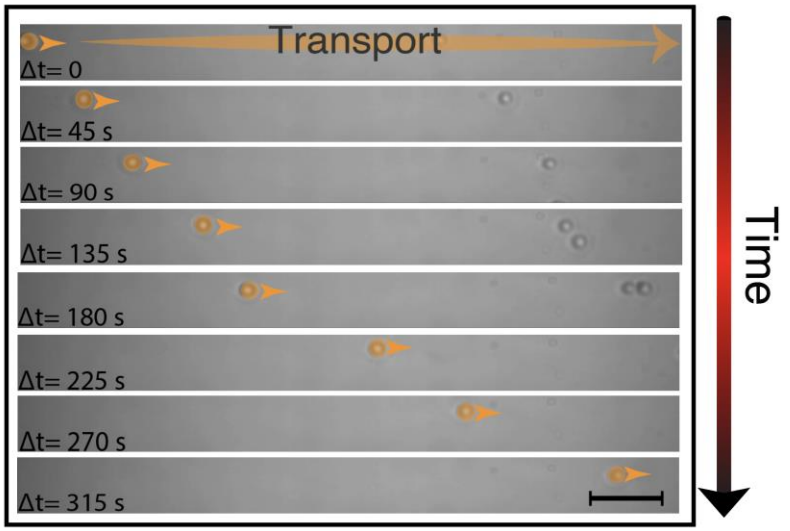

Figure 4.3: Snapshots of track of a labeled particle as propelled within the line trap with the average speed of v = 2.5 μm/s for I = 4 μW·μm−2 illuminated with the left-handed circularly polarized light at 1064 nm (Shanei, Engay, et al.).

Due to the printed phase gradient, a transverse displacement occurred in the focal line, as shown in the simulation results of Fig. 4.4. It can be observed that as the phase gradient rate increase, the line also move toward the metasurface. The displacements cause a reduction in the efficiency of metalens at the target trapping plane.

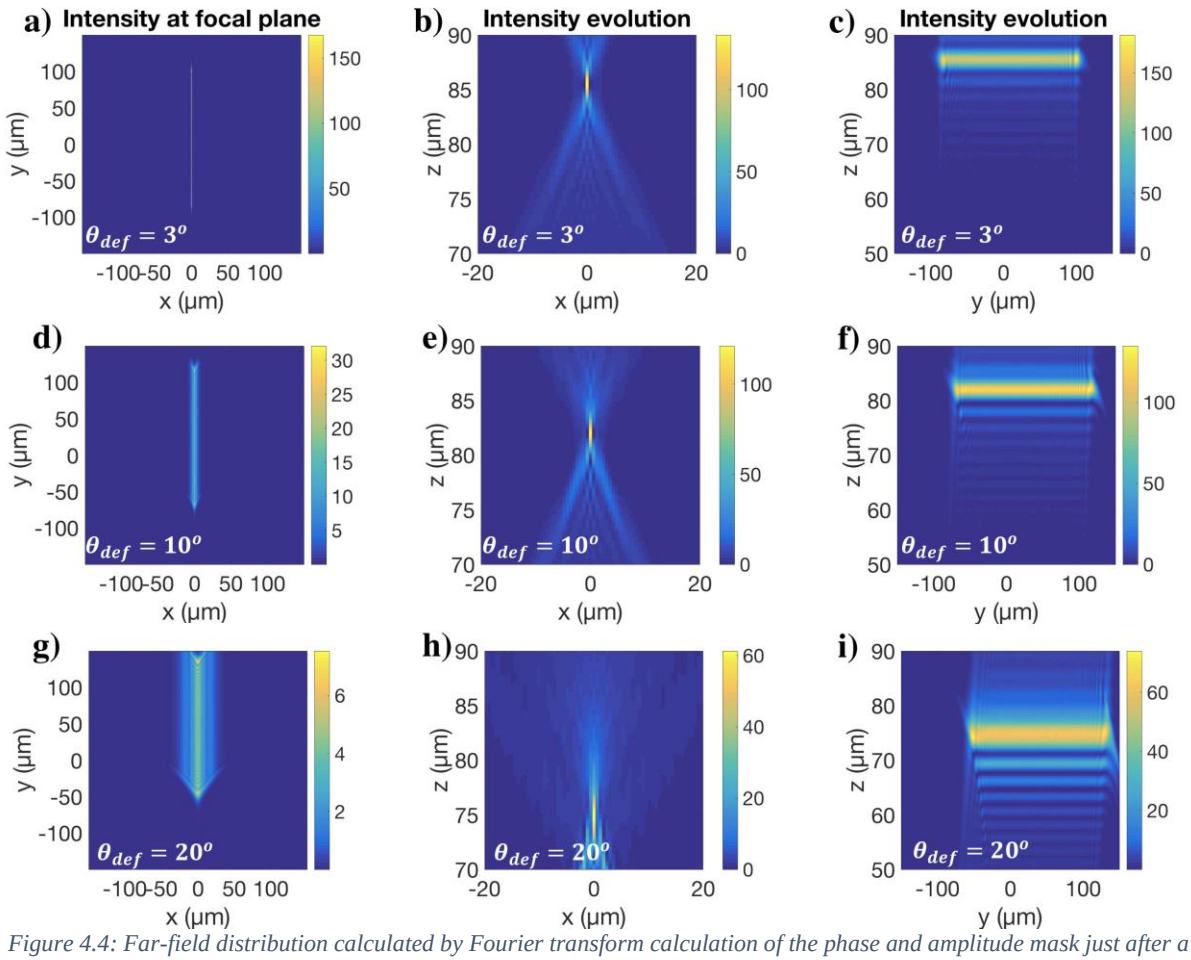

Figure 4.4: Far-field distribution calculated by Fourier transform calculation of the phase and amplitude mask just after a cylindrical metalens with the focal distance of 85 μm and meta-deflector at different planes for the deflection angles of 3º, 10º and 20º shown in the top, middle and bottom panel (Shanei, et al.).

4.2. Linear momentum manipulation

As discussed in 2.5.2, two techniques to define a meta-deflector are using a phase gradient metasurface consisting of a super-cell with a few numbers of unicells that can cover 2π phase shifts. Another approach to manipulating the wavevector of the incident field is defining a binary grating that can mimic the performance of conventional blazed grating. Figs. 4.5 (a) and (b) present the SEM images of these two beam deflectors for the deflection angle of 11º and 60º, as shown in the far-field FDTD simulation of Fig 4.5 (c). Usually, the grating defined by binary grating can have a higher deflection angle and efficiency due to the smaller lattice constant in comparison with the size of the supercell in phase gradient meta-deflectors. Figure 4.5 (d) illustrates a movable meta-structure that can convert linear momentum changes to the optical translation forces, as shown in the snapshots of Fig 4.5 (e).

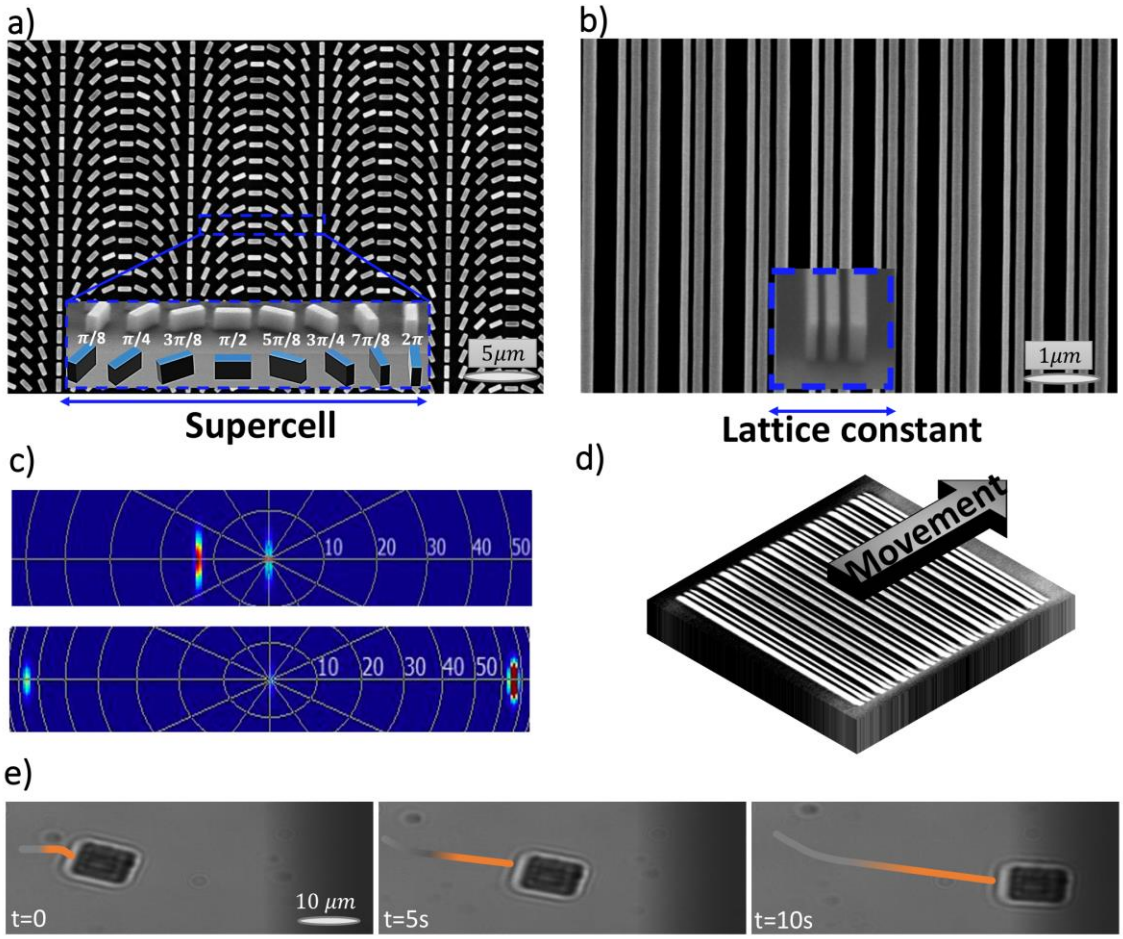

Figure 4.5: Beam deflectors based on (a) phase gradient and (b) binary blaze grating metasurfaces with (c) the deflection angles of 11° and 60° calculated by FDTD simulations in the far-field for 1064 nm laser source with left-handed circularly and linear polarized light. (d) A meta-particle consists of the binary gratings of (b). (e) Snapshots of translation of the meta-particle (illustrated in (d)) with an average speed of 4 μm/s. The particle is excited at 1064 nm with linearly polarized light and $I = 1\ \mu W \cdot \mu m^{-2}$ *(Shanei, Engay, Mylnikov, et al., unpublished data).*

The linear momentum can also be implemented to rotate particles and micro-swimmer. Different approaches have been used to rotate an object with a linearly polarized plane wave, such as implementing a chiral or birefringent structure, breaking the symmetry of objects, or uneven light-matter interaction in different sections of a particle. Figure 4.6 shows that when a spatial dependency is added by placing different grating orientations, the interaction of the incident light and the target object can generate an optical torque. For instance, the particle shown in Fig 4.6 can rotate with a linearly polarized light because of different light interactions at each arm.

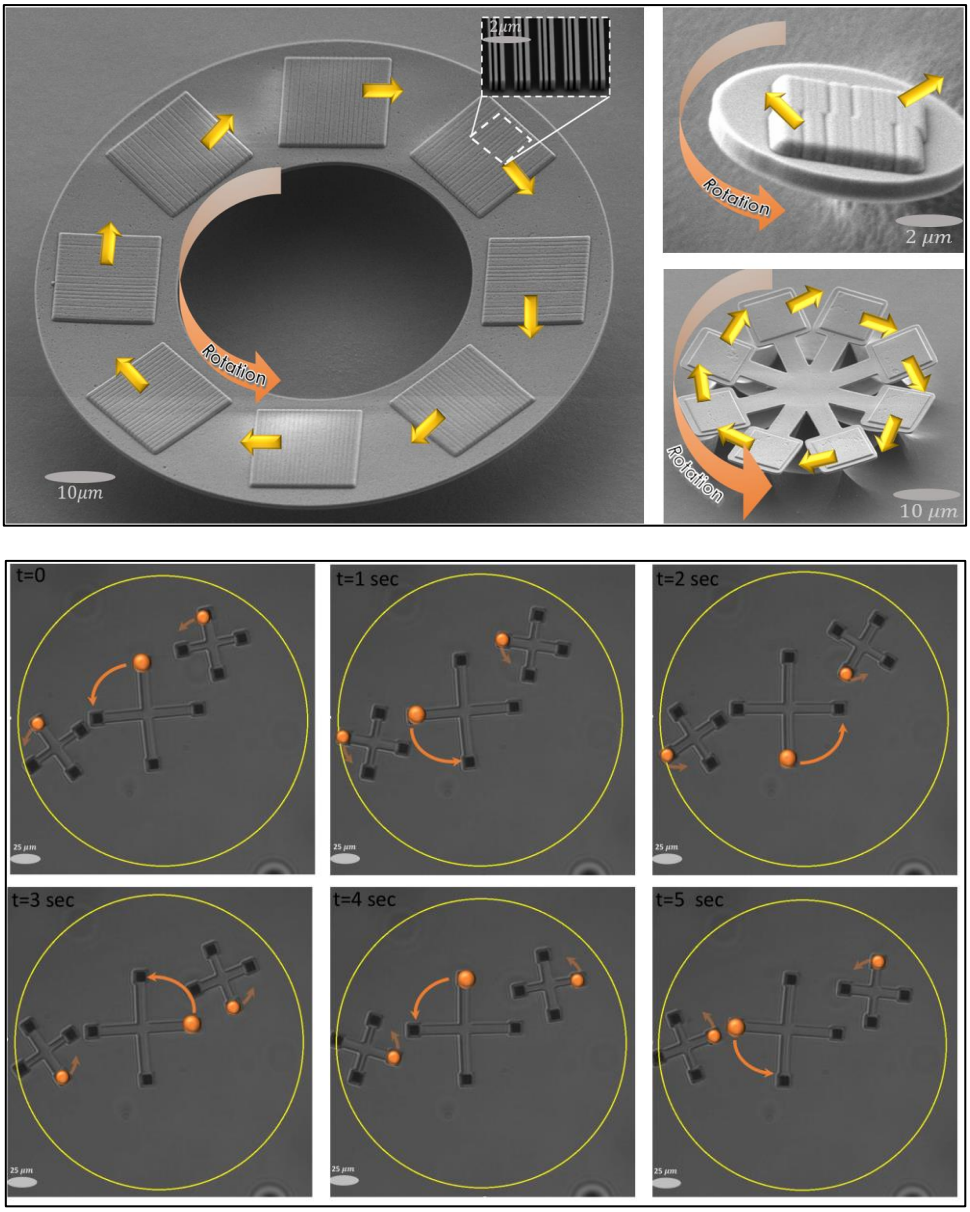

Figure 4.6: Top box: SEM images of different particles with embedded meta-grating that deflect light and rotate particles in the direction shown with yellow and orange arrows. Left: Doughnut-shaped particle with an outer diameter of 100 μm equipped with squared meta-grating with a size of 15 μm. Top right: Circular meta-particle with a diameter of 8 μm consists of two meta-grating. Bottom right: Star-shaped particle with the size of 60 μm and 8 μm squared grating at each arm. Bottom box: Snapshots of the rotation of three meta-drones inside the chamber assembled by a double-sided adhesive tape as a spacer and two cover glasses. The drones were excited from the top side by a linearly polarized Gaussian beam with a wavelength of 1064 nm, a power of 900 mW, and a beam size of 180 μm, as illustrated with the yellow circle. The larger drone at the center of the beam rotates at a higher rate (0.25 Hz) than the smaller drones at the lower intensities of the beam (0.16 Hz) (Shanei, et al., unpublished data).

4.3. Angular momentum manipulation

Helical optical beam that carries an orbital momentum is usually constructed using spatial light modulators or bulky spiral plates. Vortex beam generator-based metasurfaces have been introduced as a compact replacement during the past few years. By printing the required phase profile on the arrangement of the metasurface, a plane wave can be converted to Laguerre–Gaussian possessing an angular momentum. Fig. 4.7 shows the spiral phase profile required for a simple vortex beam generator and the addition of the axicon and lens profile which is needed for a perfect vortex beam metasurface. Perfect vortex beam metasurfaces can generate beams that propagate with annular intensities that remains fixed in size with propagation distance, as shown in the middle panel of Fig. 4.7. The third panel in Fig. 4.7 demonstrates the optical images of spiral metasurfaces with

topological charges of 2, 4 and 8 together with a SEM image related to $l = 2$. Topological charges can play an important role as a knob to tune the optical torque.
A vortex metasurface can also facilitate the spinning of a trapped particle around its optical axis. This can be achieved by adding a focusing phase profile to the Laguerre–Gaussian beam generator. In this case, the radius of the bright field at the target plane can be changed by modifying the focal distance.

As discussed, a metasurface can also be subject to momentum exchange. Hence, momentum changes before and after the structure can exert an angular momentum to a movable vortex beam generator metasurface. However, it is challenging to rotate meta-particles due to the drag force and friction.

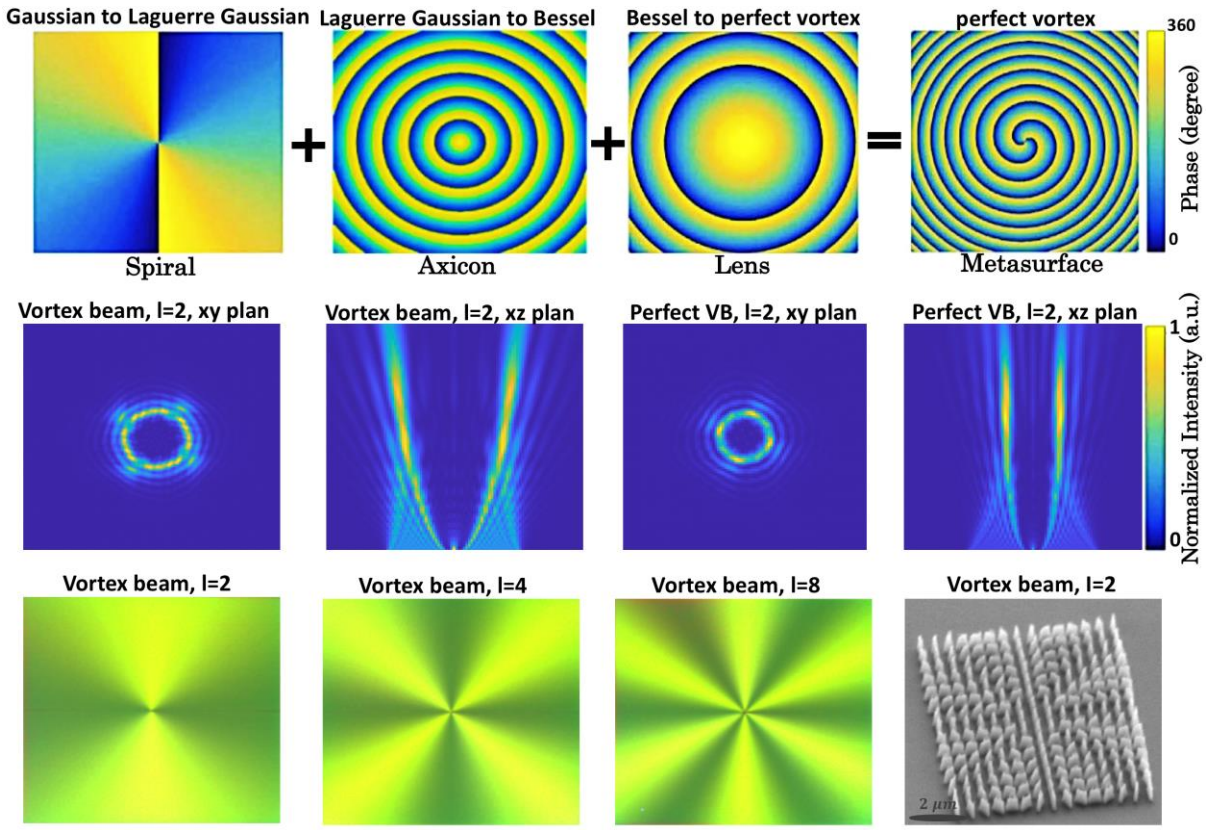

Figure 4.7: Top panel shows the spiral phase profile to construct a Laguerre Gaussian beam. The addition of an axicon phase profile and focusing can reach a perfect vortex beam generator metasurfaces. Vortex and perfect vortex beam with the topological charge of 2 at xy and xz-plane. The third panel demonstrates the optical images of a spiral metasurface with topological charges of 2, 4 and 8, together with a SEM image related to $l = 2$ (Shanei, et al., unpublished data).

4.4. Spatial distribution of light

Like a metalens with engineered spatial distribution, meta-hologram provides complicated patterns even in three-dimension. The metasurfaces are a good candidate to introduce amplitude and phase masks for holographic optical tweezers. A simple phase-only holographic metasurface can be designed by considering the field distribution with the Fraunhofer diffraction theory. To provide more flexibility in manipulating the particles, computer-generated holography (CGH) has been developed to define amplitude and phase masks which can later be implemented by the arrangement of meta-atoms. Figure 4.8 shows the target phase and amplitude profiles used to feed the CGH algorithm. The CGH algorithm generates a phase profile to reconstruct the main amplitude and phase profile. Figure 4.8 shows two different reconstruction models (calculated by Qiang Jiang from the Beijing Institute of Technology) based on the amplitude and phase quality at the target planes. The optical images of fabricated metasurfaces for each model have been shown in Fig. 4.8.

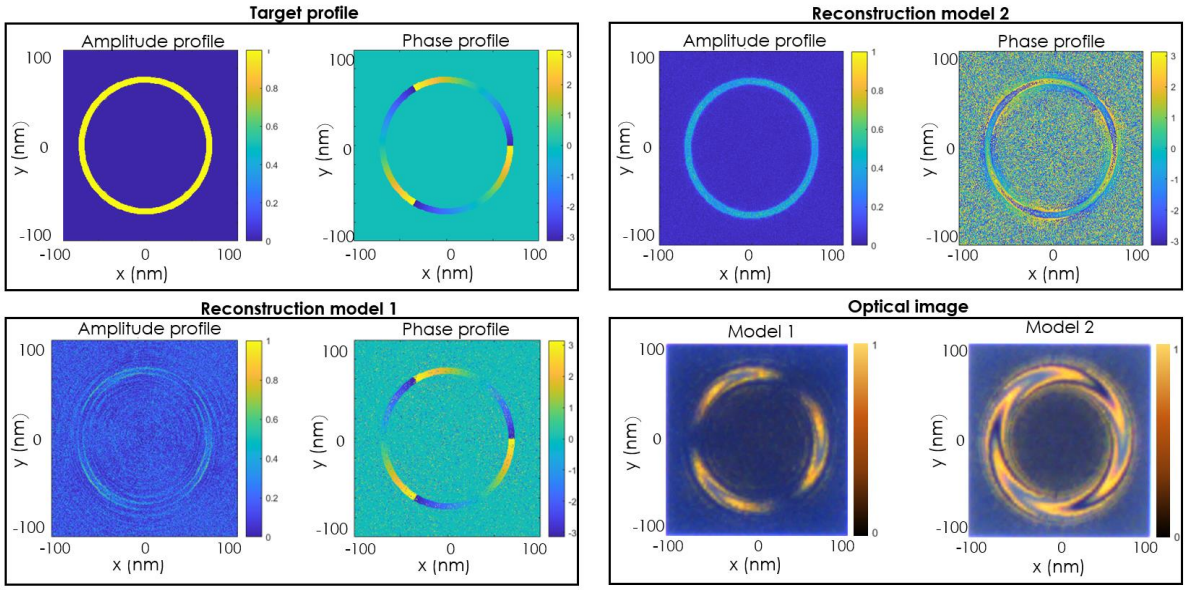

Figure 4.8: Target phase and amplitude profiles to construct with a 0 to 6π phase gradient along the circular path of the focused ring. Two reconstruction models related to the quality of amplitude and phase at the image plane. Model 1 has a uniform phase profile with some variations in the amplitude profile, and model 2 demonstrates a constant amplitude with a more distributed phase profile. Intensity contrast optical images captured at the image plane of metasurfaces for models 1 and 2 (Shanei, Jiang, et al., unpublished data).

Chapter 5

Research methods

5.1. Numerical Simulations

5.1.1. Finite-difference time-domain (FDTD) calculations

Numerical calculation plays an indispensable role in the optimization and calculation of metasurfaces. This calculation provides different benefits, from optimizing meta-atoms to investigating the performance of metasurface. Various approaches have been used to do this numerical calculation. While many electromagnetic simulations are based on solving Maxwell's equations in the frequency domain, FDTD calculates the electromagnetic field values progress at discrete steps in time. More detail about the advantages of this technique can be found in [112].
In the general case, to optimize the metasurface building block, a geometrical shape with a material composition will be defined in the FDTD simulator. Then, usually, a period boundary condition has been set in the plane parallel to the metasurface, and a perfectly matched layer as an absorbing layer in the light propagation direction.

5.1.2. Rayleigh–Sommerfeld diffraction calculations

The diffraction of waves can be calculated by scalar and vector diffraction solutions. In scalar diffraction theory, only the scalar amplitude of one transverse component of the field has been considered to calculate the field propagation. The scalar diffraction can provide accurate results about the trace of the field by considering different approximation conditions, such as propagating in a linear, isotropic and homogeneous medium. Also, this is important that the distance between the diffracting aperture and the observing plane is larger than the electromagnetic field's working wavelength.
The Rayleigh-Sommerfeld diffraction (RSD) integral calculates scalar wave propagation. In contrast to approximations such as Fresnel or Fraunhofer diffraction, the RSD gives an exact scalar solution for the diffracted beam of a given input field. RSD states that each point in the source plane emits secondary spherical wavelets. To find the field at the target plane, it is required to add the contributions from all point sources together, which corresponds to the Huygens-Fresnel principle.

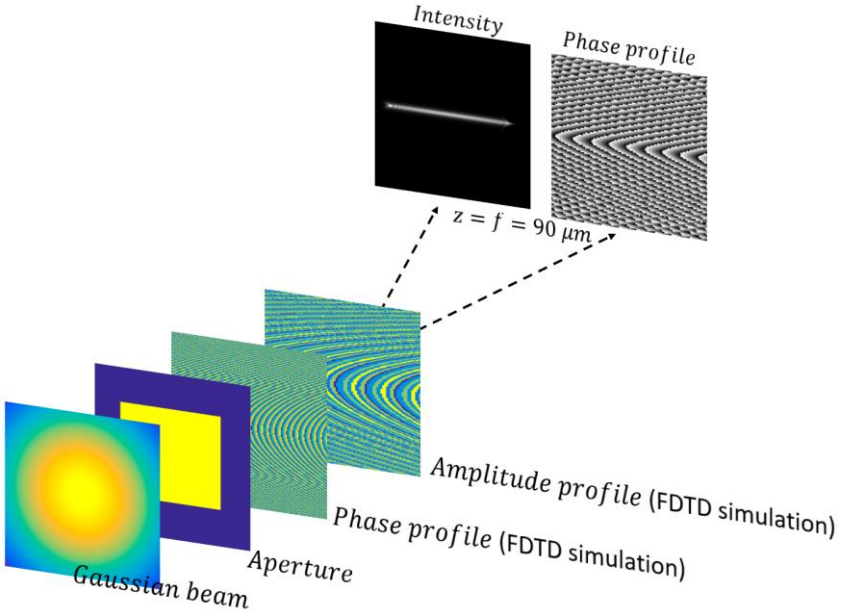

Figure 5.1: Implementing a Fourier transform to calculate a far-field projection of a Gaussian beam after traveling through an aperture with the size of a metasurface and filtering with the amplitude and phase masks.

5.2. Micro and Nanofabrication

Micro and nanofabrication can be considered as the basis of manufacturing for most of the modern miniaturized systems used in our daily lives, such as computer chips and detectors, mobile phones, medical instruments, and more. Micro and nanofabrication include a series of processes to shape a substrate in an additive or subtractive technique into a complex structure with engineered materials. These techniques are divided into two primary approaches. One is breaking a bulk material into desired micro and nano-scale pieces through physical and chemical processes. The approach is forming a micro and nano-scale structure using materials in atomic and molecular sizes as the building block. The top-down nanofabrication method fabricates the structures in this report with negative and positive electron-sensitive resists.

5.2.1. Deposition

In nanofabrication, different methods are used to deposit thin films. These methods are divided into chemical vapor deposition (CVD) and physical vapor deposition (PVD). In CVD, heat or plasma facilitates chemical reactions between a heated substrate and a mixture of desired gases. PVD is a process where a solid material is evaporated and deposited on substrates at very low-pressure chambers. The two main PVD techniques used to fabricate structures in this report are thermal evaporation and sputtering. The required heating energy to evaporate a solid source in thermal evaporation can be provided either by an electron beam or induction. In the sputtering deposition, the vaporized atoms are commonly produced through the collision of plasma ions and solid targets. Figure 5.2 shows the spectra of the refractive index and extinction coefficient of the a-Si layer used for fabrication in this thesis.

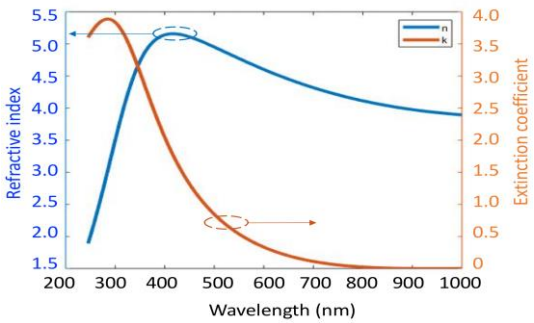

Figure 5.2: Real and imaginary parts of the dielectric function of the deposited a-Si in low pressure through CVD (measured by Woollam M2000 Ellipsometer, Shanei et al.).

5.2.2. Electron beam lithography

In top-down nanofabrication, lithography is crucial in transferring patterns to the resist. In electron beam lithography (EBL), a scanning tightly focused beam of electrons is used to pattern a surface of a resist-covered substrate with a minimum feature size of 10 nm. By submerging the exposed area into a proper developer, a negative or positive image will be observed on the covered substrate following the tone of the e-beam resist. After development, the final structure can be achieved by either etching the substrate or depositing the target material.

5.2.3. Etching

Etching is an important step in nanofabrication to transfer a pattern into a substrate covered by a mask. The masking materials that protect the underlying substrate are divided into two categories. The first one is soft etching masks, which are the photo and electron resists patterned during lithography. The second consists of hard materials that are more durable masks, such as silicon oxide and metals. In nanofabrication, the etching processes are divided into wet and dry techniques that utilize liquid chemicals and gases as etchant material. In wet etching, the sample is submerged in a liquid while the accelerated ionized molecules of an etching gas are implemented to complete the dry etching process.
In this report, the inductively coupled plasma reactive ion etching (ICP-RIE) method is used to transfer the pattern of metasurfaces into the substrate. The ICP-RIE technique is a combination of chemical and physical etching that provides the possibility of isotropic and anisotropic material removal. An example of isotropic and anisotropic etching is shown in Fig. 5.3.

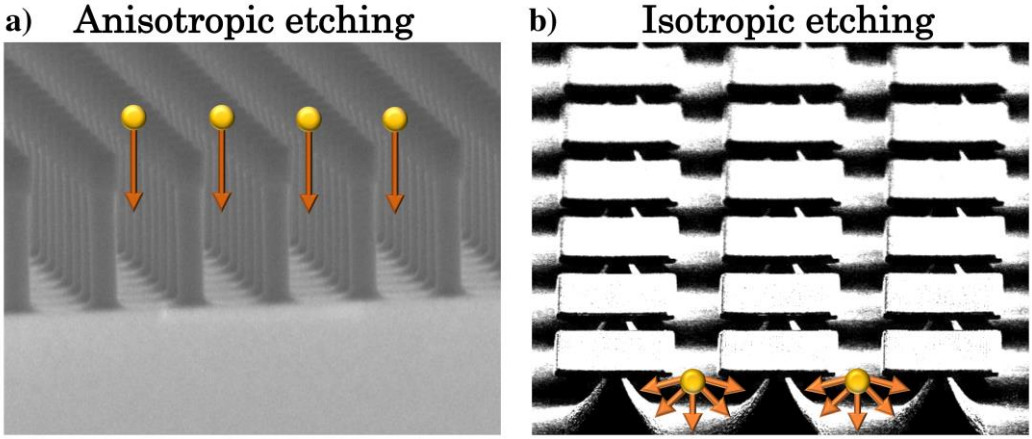

Figure 5.3: (a) Anisotropic etching to fabricate a high aspect ratio of a-Si nano bars with a thickness of 980 nm using SF_6 at cryogenic temperature. (b) Isotropic etching of a-Si to release a 1 μm SiO_2 particle with embedded metasurface that is covered with 60 nm of Nickel as a hard mask (fabricated by M. Shanei at Chakmers MC2 cleanroom).

Figure 5.4 shows some SEM images of unsuccessful attempts during the optimization of the nanofabrication processes. These images are related to three different structures of nanofins, asymmetric dimmers, and trinary gratings.

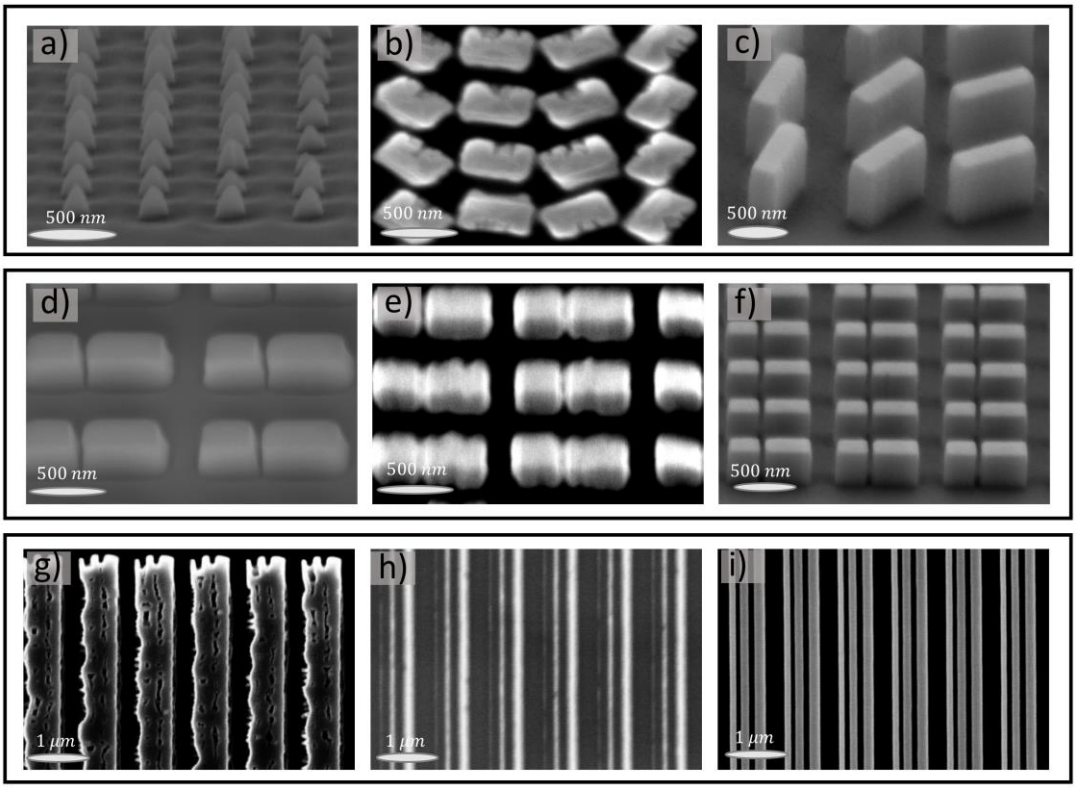

Figure 5.4: Failed attempts in fabricating silicon-based metasurfaces and final structures. (a)-(c) Metaatoms with a rectangular cross-section. In (a), a low ratio between forward and inductively coupled plasma power can shape a pyramidal cross-section. In (b), a low working pressure inside the etching machine generates some sparks with high ion energy that causes some notches into the nanofins. (c) Nanofins with vertical side-wall and rectangular cross-sections. (d)-(f) Asymmetric dimmers. (d) Different gap sizes between the dimmers at the top and bottom due to low forward power in etching. (c) Low resolution in the edges of dimmers due to charge accumulation during the EBL exposure. (f) Final structure with a uniform gap size of 50 nm between the dimmers. (g)-(i) Optimizing EBL dose for grating fabrication with three parallel solid rigid using a negative resist. (g) lower, (h) higher, and (i) optimum doses needed for the fabrication of grating with the defined gap sizes of 70 nm (fabricated by M. Shanei at Chakmers MC2 cleanroom).

To summarize this section, a schematic from different steps in the fabrication process of metasurfaces has been illustrated in Fig. 5.5 for positive and negative resists.

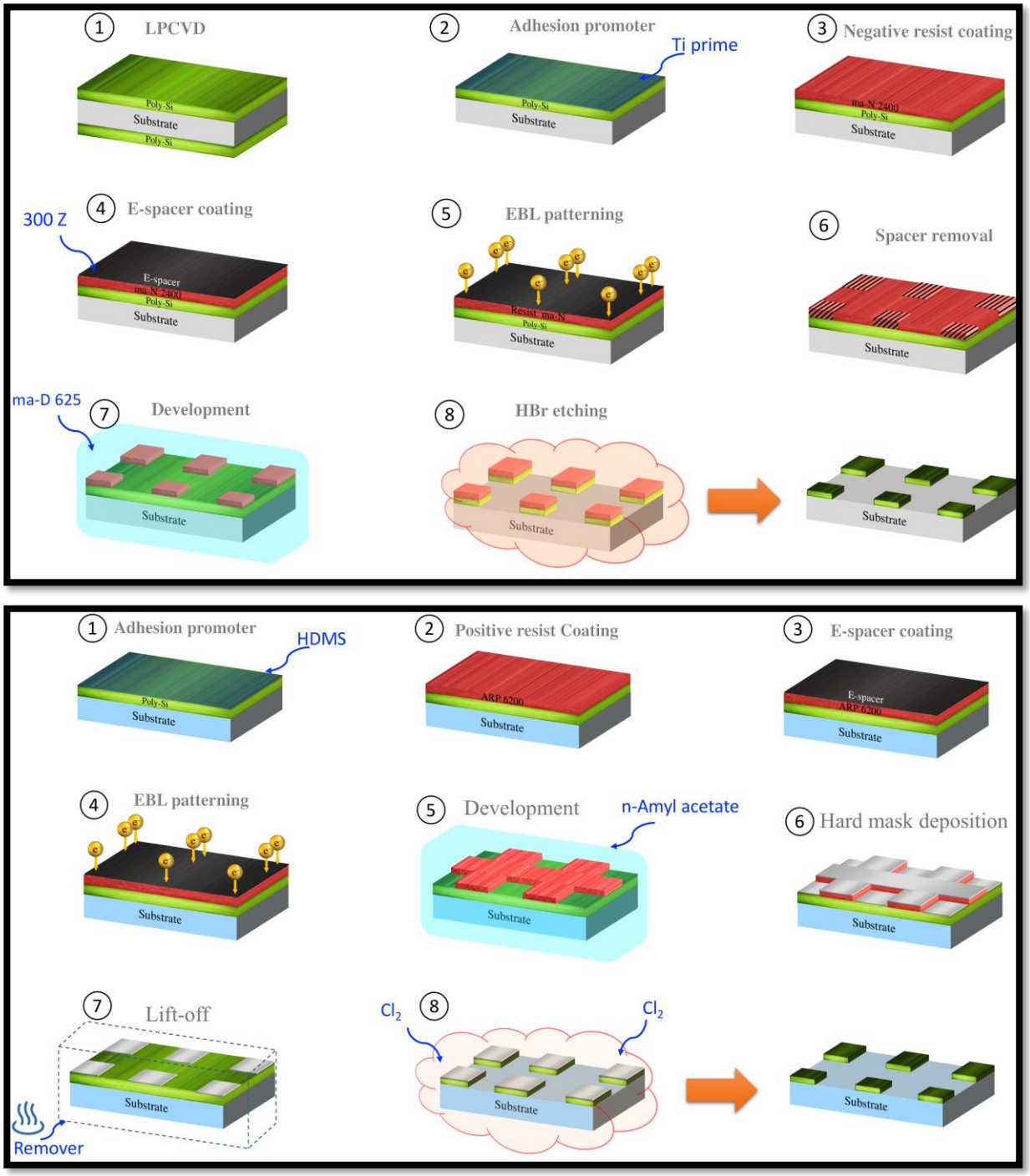

Figure 5.5: Summary of two nano-fabrication techniques using negative and positive resist in the top and bottom boxes. Since the silicon layer can adsorb water molecules from the humidity of the environment, its surface is usually hydrophilic. So, to enhance the adhesion between the substrate and coated resist, it is suggested to use some promoters such as Ti prime and Hexamethyldisilazane (HMDS) for the negative and positive resist coating, respectively. Due to the charge accumulation in the dielectric substrate, such as SiO_2, during EBL, it is required to enhance the conductivity of the sample by coating a conductive polymer or deposition of a thin layer of metal. During the EBL and development processes, the required pattern is transferred to the resist, and then, the etching process defines the final metasurface. The negative resist in the etching process can also use as a soft mask that can protect the covered layer (silicon). Hence, this process does not need any hard mask deposition and lift-off process.

5.3. Optical Characterization

5.3.1. Measurements of polarization conversion efficiency

As discussed in section 2, it is crucial for metasurfaces to have high efficiency in terms of transmission or reflection. Hence, efficiency is an important merit to consider in phase gradient metasurfaces as a competitor with bulky optical elements.

In PB metasurfaces that act as a half-waveplate, one-handedness of the polarization switches to the other and acquires the required phase shifts. Therefore, the ability of each unit cell to convert the handedness of the incident light is defined as polarization conversion efficiency (PCE).

To experimentally measure the PCE of a metasurface, a periodic array of meta-atoms oriented at 45° was placed between two crossed linear polarizers. This measurement is identical to sending an RCP (LCP) and monitoring LCP (RCP) after PB patterns. Since the measured spectrum from the spectrophotometer consists of different signals, such as the light source profile (I_{white}), the background glass signal (I_{Bck}), and the dark signal (I_{Dark}), the captured signal should be calibrated using

$$T_{co} = \frac{I_{co} - I_{Dark}}{I_{white} - I_{Dark}} \tag{5.1}$$

$$T_{cross} = \frac{I_{cross} - I_{Bck}}{I_{white} - I_{Dark}}. \tag{5.2}$$

I_{co} and I_{cross} are the intensities of the transmitted beam from the metasurface for the same and orthogonal polarization states before and after the metasurface, respectively.

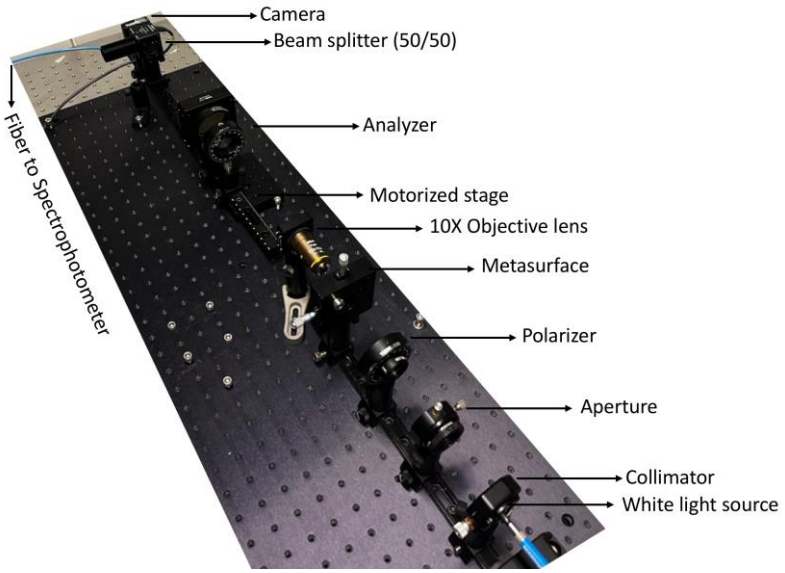

FIGURE 5.6: Optical setup for the polarization conversion efficiency measurements.

5.3.2. Optical manipulation measurements

The optical setup used for trapping and manipulating 2-μm particles (microParticles GmbH) is shown in Fig5.5. As shown in the inset, the light impinges the metasurface from the backside and then prints the particles to the cover glass on the other side. So, the particles sediment after a while due to the scattering force of the 1064 nm laser (Cobolt Rumba, = 1 mm) and gravity. The metalens is in contact with particles in a sample chamber, assembled by adhering the metasurface substrate to a microscope cover glass using a spacer with a nominal thickness of 100 μm.

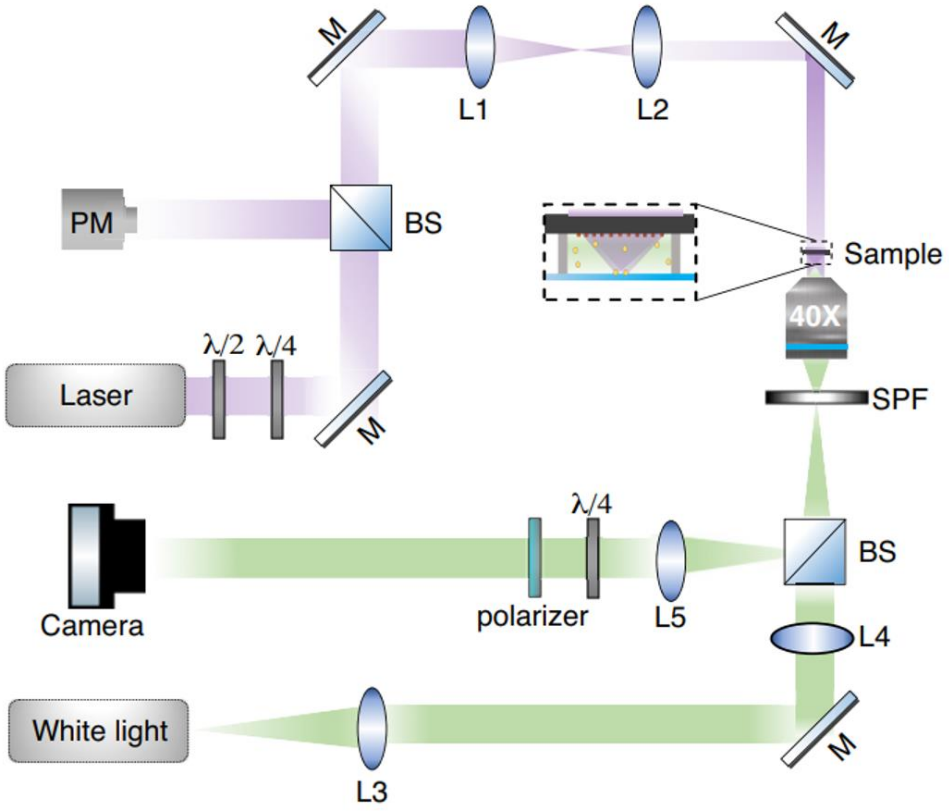

Figure 5.7. Optical trapping setup. L1-L5, lenses; M, plane mirror; λ/2, HWP; λ/4, QWP; BS, beam splitter; SPF, short-pass filter; 40× objective (NA = 0.9); camera (Thorlabs, CCD).

Chapter 6

Concluding remarks

Flat optics with ultra-thin planar metasurface can tailor polarization, amplitude, and phase of the incident wavefront. In Chapter 2, the fundamental principle of metasurfaces was discussed by categorizing it into different types such as working wavelength, constitution material, design methodologies, etc. Chapter 3 was dedicated to presenting a review of field-driven manipulation of micro-object focusing on the optical field's powerful actuation mechanisms. It was shown that the momentum exchange between a beam of light and structure plays an important role in manipulating the objects. Chapter 4 presented some applications of metasurfaces in the compact manipulation of objects enabled by engineering different degrees of freedom of light. Lastly, Chapter 6 was dedicated to the research method methods such as the numerical simulation to optimize metasurface structure and field propagation calculation, the nanofabrication processes of metasurfaces and required optical setups for characterization of metasurfaces.

6.1. Summary of appended paper

In this paper, an ultrathin cylindrical metasurface is designed and fabricated to trap and push particles along its focal line. The required phase profile was experimentally realized using arrays of nanofins with locally varying rotation angles (PB method). The metasurface is optimized to work at λ=1064 and with amorphous silicon (a-Si) building blocks arranged in a square lattice on a glass substrate. As discussed in Chapter 3, the confinement achieved through the intensity gradient in the transverse plane pointed to the focal line. So, the particles outside the focal area move laterally toward the trapping line. Then, the trapped particles move in the expected direction due to the phase gradient but with a discontinuation motion due to the existence of the intensity hot spots in the focal line. We found that the beam deflector phase gradient adds unwanted intensity fluctuations that tended to lock particles to specific positions. To decrease the influence of the intensity hotspots, the target plane was located in the defocusing plane of the metalens. Due to diffraction effects, a relatively smooth intensity distribution has been observed in the translation of the particles.

6.2. Outlook

The study of microscopic particles in suspension has significantly impacted science and engineering. For example, the quantification of thermal Brownian motion was the main experiment that convinced the existence of atoms. Hence, studying of collective interactions of artificial swimmers, such as meta-particles, can be useful in describing interactions ranging from molecular machines to atmospheric dynamics. This can be observed if a metasurface is incorporated into a micro-scale object allowed to move freely across a surface.

Optical tweezers are used to manipulate particles with sizes of 100 nm to 10 μm with the driving forces in the scale of piconewton. However, the manipulations of larger particles are challenging due to gravity and inertia, studying the possibility of manipulating meta-particles that can present a potential application, such as the collection of absorptive or nanoscale particles, acceleration of detection rate of the analysts.

References

[1] Potyrailo, Radislav A., Ravi K. Bonam, John G. Hartley, Timothy A. Starkey, Peter Vukusic, Milana Vasudev, Timothy Bunning et al. "Towards outperforming conventional sensor arrays with fabricated individual photonic vapour sensors inspired by Morpho butterflies." *Nature communications* **6**, no. 1 (2015): 7959.

[2] Huo, Pengcheng, Si Zhang, Yuzhang Liang, Yanqing Lu, and Ting Xu. "Hyperbolic metamaterials and metasurfaces: fundamentals and applications." *Advanced Optical Materials* **7**, no. 14 (2019): 1801616.

[3] Dong, Yuan, Zhengji Xu, Nanxi Li, Jinchao Tong, Yuan Hsing Fu, Yanyan Zhou, Ting Hu et al. "Si metasurface half-wave plates demonstrated on a 12-inch CMOS platform." *Nanophotonics* **9**, no. 1 (2020): 149-157.

[4] Ashkin, Arthur. "Optical trapping and manipulation of neutral particles using lasers." *Proceedings of the National Academy of Sciences* **94**, no. 10 (1997): 4853-4860.

[5] Yu, Nanfang, Patrice Genevet, Mikhail A. Kats, Francesco Aieta, Jean-Philippe Tetienne, Federico Capasso, and Zeno Gaburro. "Light propagation with phase discontinuities: generalized laws of reflection and refraction." *Science* **334**, no. 6054 (2011): 333-337.

[6] Capasso, Federico. "The future and promise of flat optics: a personal perspective." *Nanophotonics* **7**, no. 6 (2018): 953-957.

[7] Cui, Tie Jun, Shuo Liu, and Lei Zhang. "Information metamaterials and metasurfaces." *Journal of materials chemistry C* **5**, no. 15 (2017): 3644-3668.

[8] Holloway, Christopher L., Edward F. Kuester, Joshua A. Gordon, John O'Hara, Jim Booth, and David R. Smith. "An overview of the theory and applications of metasurfaces: The two-dimensional equivalents of metamaterials." *IEEE antennas and propagation magazine* **54**, no. 2 (2012): 10-35.

[9] Hu, Jie, Sankhyabrata Bandyopadhyay, Yu-hui Liu, and Li-yang Shao. "A review on metasurface: from principle to smart metadevices." *Frontiers in Physics* **8**, (2021): 586087.

[10] Hsu, Wei-Lun, Yen-Chun Chen, Shang Ping Yeh, Qiu-Chun Zeng, Yao-Wei Huang, and Chih-Ming Wang. "Review of metasurfaces and metadevices: advantages of different materials and fabrications." *Nanomaterials* **12**, no. 12 (2022): 1973.

[11] Li, Jing, Tiesheng Wu, Wenbin Xu, Yumin Liu, Chang Liu, Yu Wang, Zhongyuan Yu, Danfeng Zhu, Li Yu, and Han Ye. "Mechanisms of 2π phase control in dielectric metasurface and transmission enhancement effect." *Optics Express* **27**, no. 16 (2019): 23186-23196.

[12] Zhou, Hongping, Lei Chen, Fei Shen, Kai Guo, and Zhongyi Guo. "Broadband achromatic metalens in the midinfrared range." *Physical Review Applied* **11**, no. 2 (2019): 024066.

[13] Arbabi, Amir, Yu Horie, Mahmood Bagheri, and Andrei Faraon. "Dielectric metasurfaces for complete control of phase and polarization with subwavelength spatial resolution and high transmission." *Nature nanotechnology* **10**, no. 11 (2015): 937-943.

[14] Schonbrun, Ethan, Kwanyong Seo, and Kenneth B. Crozier. "Reconfigurable imaging systems using elliptical nanowires." *Nano letters* **11**, no. 10 (2011): 4299-4303.

[15] Khorasaninejad, Mohammadreza, Alexander Yutong Zhu, Charles Roques-Carmes, Wei Ting Chen, Jaewon Oh, Ishan Mishra, Robert C. Devlin, and Federico Capasso.

"Polarization-insensitive metalenses at visible wavelengths." *Nano letters* **16**, no. 11 (2016): 7229-7234.

[16] Sun, Shulin, Kuang-Yu Yang, Chih-Ming Wang, Ta-Ko Juan, Wei Ting Chen, Chun Yen Liao, Qiong He et al. "High-efficiency broadband anomalous reflection by gradient meta-surfaces." *Nano letters* **12**, no. 12 (2012): 6223-6229.

[17] Ginn, James C., Igal Brener, David W. Peters, Joel R. Wendt, Jeffrey O. Stevens, Paul F. Hines, Lorena I. Basilio et al. "Realizing optical magnetism from dielectric metamaterials." *Physical review letters* **108**, no. 9 (2012): 097402.

[18] Decker, Manuel, Isabelle Staude, Matthias Falkner, Jason Dominguez, Dragomir N. Neshev, Igal Brener, Thomas Pertsch, and Yuri S. Kivshar. "High-efficiency dielectric Huygens' surfaces." *Advanced Optical Materials* **3**, no. 6 (2015): 813-820.

[19] Geffrin, Jean-Michel, B. García-Cámara, Raquel Gómez-Medina, Pablo Albella, L. S. Froufe-Pérez, Christelle Eyraud, Amelie Litman et al. "Magnetic and electric coherence in forward-and back-scattered electromagnetic waves by a single dielectric subwavelength sphere." *Nature communications* **3**, no. 1 (2012): 1171.

[20] Chong, Katie E., Lei Wang, Isabelle Staude, Anthony R. James, Jason Dominguez, Sheng Liu, Ganapathi S. Subramania et al. "Efficient polarization-insensitive complex wavefront control using Huygens' metasurfaces based on dielectric resonant meta-atoms." *Acs Photonics* **3**, no. 4 (2016): 514-519.

[21] Pancharatnam, Shivaramakrishnan. "Generalized theory of interference and its applications: Part II. Partially coherent pencils." In *Proceedings of the Indian Academy of Sciences-Section A*, vol. **44**, no. 6, pp. 398-417. New Delhi: Springer India, 1956.

[22] Cerjan, Alexander, and Shanhui Fan. "Achieving arbitrary control over pairs of polarization states using complex birefringent metamaterials." *Physical review letters* **118**, no. 25 (2017): 253902.

[23] Wang, Jian, and Jing Du. "Plasmonic and dielectric metasurfaces: design, fabrication and applications." *Applied Sciences* **6**, no. 9 (2016): 239.

[24] Sun, Shulin, Qiong He, Shiyi Xiao, Qin Xu, Xin Li, and Lei Zhou. "Gradient-index meta-surfaces as a bridge linking propagating waves and surface waves." *Nature materials* **11**, no. 5 (2012): 426-431.

[25] Cao, Wei, Xiaodong Yang, and Jie Gao. "Broadband polarization conversion with anisotropic plasmonic metasurfaces." *Scientific reports* **7**, no. 1 (2017): 1-9.

[26] Segal, Nadav, Shay Keren-Zur, Netta Hendler, and Tal Ellenbogen. "Controlling light with metamaterial-based nonlinear photonic crystals." *Nature Photonics* **9**, no. 3 (2015): 180-184.

[27] Hassanfiroozi, Amir, Po-Sheng Huang, Shih-Hsiu Huang, Kuang-I. Lin, Yu-Tsung Lin, Chien-Feng Chien, Yuzhi Shi, Wen-Jen Lee, and Pin Chieh Wu. "A Toroidal-Fano-Resonant Metasurface with Optimal Cross-Polarization Efficiency and Switchable Nonlinearity in the Near-Infrared." *Advanced Optical Materials* **9**, no. 21 (2021): 2101007.

[28] Li, Lin, Zexuan Liu, Xifeng Ren, Shuming Wang, Vin-Cent Su, Mu-Ku Chen, Cheng Hung Chu et al. "Metalens-array–based high-dimensional and multiphoton quantum source." *Science* **368**, no. 6498 (2020): 1487-1490.

[29] Mueller, JP Balthasar, Noah A. Rubin, Robert C. Devlin, Benedikt Groever, and Federico Capasso. "Metasurface polarization optics: independent phase control of arbitrary orthogonal states of polarization." *Physical review letters* **118**, no. 11 (2017): 113901.

[30] Khorasaninejad, Mohammadreza, Wei Ting Chen, Robert C. Devlin, Jaewon Oh, Alexander Y. Zhu, and Federico Capasso. "Metalenses at visible wavelengths:

Diffraction-limited focusing and subwavelength resolution imaging." *Science* **352**, no. 6290 (2016): 1190-1194.

[31] Khorasaninejad, Mohammadreza, Alexander Yutong Zhu, Charles Roques-Carmes, Wei Ting Chen, Jaewon Oh, Ishan Mishra, Robert C. Devlin, and Federico Capasso. "Polarization-insensitive metalenses at visible wavelengths." *Nano letters* **16**, no. 11 (2016): 7229-7234.

[32] Li, Jie, Guocui Wang, Chenglong Zheng, Jitao Li, Yue Yang, Zhang Zhang, Maosheng Yang et al. "All-silicon metasurfaces for polarization multiplexed generation of terahertz photonic orbital angular momentum superposition states." *Journal of Materials Chemistry C* **9**, no. 16 (2021): 5478-5485.

[33] Kim, Joohoon, Dong Kyo Oh, Hongyoon Kim, Gwanho Yoon, Chunghwan Jung, Jaekyung Kim, Trevon Badloe et al. "Metasurface holography reaching the highest efficiency limit in the visible via one-step nanoparticle-embedded-resin printing." *Laser & Photonics Reviews* **16**, no. 8 (2022): 2200098.

[34] Yang, Jhen-Hong, Viktoriia E. Babicheva, Min-Wen Yu, Tien-Chang Lu, Tzy-Rong Lin, and Kuo-Ping Chen. "Structural colors enabled by lattice resonance on silicon nitride metasurfaces." *ACS nano* **14**, no. 5 (2020): 5678-5685.

[35] Fan, Zhi-Bin, Zeng-Kai Shao, Ming-Yuan Xie, Xiao-Ning Pang, Wen-Sheng Ruan, Fu-Li Zhao, Yu-Jie Chen, Si-Yuan Yu, and Jian-Wen Dong. "Silicon nitride metalenses for close-to-one numerical aperture and wide-angle visible imaging." *Physical Review Applied* **10**, no. 1 (2018): 014005.

[36] Wu, Yunkai, Wenhong Yang, Yubin Fan, Qinghai Song, and Shumin Xiao. "TiO2 metasurfaces: From visible planar photonics to photochemistry." *Science advances* **5**, no. 11 (2019): eaax0939.

[37] Wen, Dandan, Jasper J. Cadusch, Jiajun Meng, and Kenneth B. Crozier. "Multifunctional dielectric metasurfaces consisting of color holograms encoded into color printed images." *Advanced Functional Materials* **30**, no. 3 (2020): 1906415.

[38] Sun, Shang, Zhenxing Zhou, Chen Zhang, Yisheng Gao, Zonghui Duan, Shumin Xiao, and Qinghai Song. "All-dielectric full-color printing with TiO2 metasurfaces." *ACS nano* **11**, no. 5 (2017): 4445-4452.

[39] Lin, Yu-Tsung, Amir Hassanfiroozi, Wei-Rou Jiang, Mei-Yi Liao, Wen-Jen Lee, and Pin Chieh Wu. "Photoluminescence enhancement with all-dielectric coherent metasurfaces." *Nanophotonics* **11**, no. 11 (2022): 2701-2709.

[40] Mueller, JP Balthasar, Noah A. Rubin, Robert C. Devlin, Benedikt Groever, and Federico Capasso. "Metasurface polarization optics: independent phase control of arbitrary orthogonal states of polarization." *Physical review letters* **118**, no. 11 (2017): 113901.

[41] Wang, Shuai, Zi-Lan Deng, Yujie Wang, Qingbin Zhou, Xiaolei Wang, Yaoyu Cao, Bai-Ou Guan, Shumin Xiao, and Xiangping Li. "Arbitrary polarization conversion dichroism metasurfaces for all-in-one full Poincaré sphere polarizers." *Light: Science & Applications* **10**, no. 1 (2021): 24.

[42] Park, Joon-Suh, Shuyan Zhang, Alan She, Wei Ting Chen, Peng Lin, Kerolos MA Yousef, Ji-Xin Cheng, and Federico Capasso. "All-glass, large metalens at visible wavelength using deep-ultraviolet projection lithography." *Nano letters* **19**, no. 12 (2019): 8673-8682.

[43] Song, Qinghua, Arthur Baroni, Rajath Sawant, Peinan Ni, Virginie Brandli, Sébastien Chenot, Stéphane Vézian et al. "Ptychography retrieval of fully polarized holograms from geometric-phase metasurfaces." *Nature communications* **11**, no. 1 (2020): 2651.

[44] Chen, Bo Han, Pin Chieh Wu, Vin-Cent Su, Yi-Chieh Lai, Cheng Hung Chu, I. Chen Lee, Jia-Wern Chen et al. "GaN metalens for pixel-level full-color routing at visible light." *Nano letters* **17**, no. 10 (2017): 6345-6352.

[45] Wang, Qiu-Hua, Pei-Nan Ni, Yi-Yang Xie, Qiang Kan, Pei-Pei Chen, Pan Fu, Jun Deng et al. "On-chip generation of structured light based on metasurface optoelectronic integration." *Laser & Photonics Reviews* **15**, no. 3 (2021): 2000385.

[46] Gao, Ramon, Michael D. Kelzenberg, Yonghwi Kim, Ognjen Ilic, and Harry A. Atwater. "Optical characterization of silicon nitride metagrating-based lightsails for self-stabilization." *ACS Photonics* **9**, no. 6 (2022): 1965-1972.

[47] Elsawy, Mahmoud MR, Stéphane Lanteri, Régis Duvigneau, Jonathan A. Fan, and Patrice Genevet. "Numerical optimization methods for metasurfaces." *Laser & Photonics Reviews* **14**, no. 10 (2020): 1900445.

[48] So, Sunae, Jungho Mun, Junghyun Park, and Junsuk Rho. "Revisiting the Design Strategies for Metasurfaces: Fundamental Physics, Optimization, and Beyond." *Advanced Materials* (2022): 2206399.

[49] Shi, Xin, Tianshuo Qiu, Jiafu Wang, Xueqing Zhao, and Shaobo Qu. "Metasurface inverse design using machine learning approaches." *Journal of Physics D: Applied Physics* **53**, no. 27 (2020): 275105.

[50] Midtvedt, Daniel, Vasilii Mylnikov, Alexander Stilgoe, Mikael Käll, Halina Rubinsztein-Dunlop, and Giovanni Volpe. "Deep learning in light–matter interactions." *Nanophotonics* **11**, no. 14 (2022): 3189-3214.

[51] Zhang, Zhengren, Dandan Wen, Chunmei Zhang, Ming Chen, Wei Wang, Shuqi Chen, and Xianzhong Chen. "Multifunctional light sword metasurface lens." *ACS photonics* **5**, no. 5 (2018): 1794-1799.

[52] Maguid, Elhanan, Igor Yulevich, Michael Yannai, Vladimir Kleiner, Mark L Brongersma, and Erez Hasman. "Multifunctional interleaved geometric-phase dielectric metasurfaces." *Light: Science & Applications* **6**, no. 8 (2017): e17027-e17027.

[53] Chen, Shuqi, Wenwei Liu, Zhancheng Li, Hua Cheng, and Jianguo Tian. "Metasurface-empowered optical multiplexing and multifunction." *Advanced Materials* **32**, no. 3 (2020): 1805912.

[54] Zhou, You, Ivan I. Kravchenko, Hao Wang, J. Ryan Nolen, Gong Gu, and Jason Valentine. "Multilayer noninteracting dielectric metasurfaces for multiwavelength metaoptics." *Nano letters* **18**, no. 12 (2018): 7529-7537.

[55] Huang, Cheng, Changlei Zhang, Jianing Yang, Bo Sun, Bo Zhao, and Xiangang Luo. "Reconfigurable metasurface for multifunctional control of electromagnetic waves." *Advanced Optical Materials* **5**, no. 22 (2017): 1700485.

[56] https://www.scientificamerican.com/article/tiny-lenses-will-enable-design-of-miniature-optical-devices.

[57] Sun, Yu. *Field-Driven Micro and Nanorobots for Biology and Medicine*. Edited by Xian Wang, and Jiangfan Yu. Springer, 2022.

[58] Hu, Mengyi, Xuemei Ge, Xuan Chen, Wenwei Mao, Xiuping Qian, and Wei-En Yuan. "Micro/nanorobot: A promising targeted drug delivery system." *Pharmaceutics* **12**, no. 7 (2020): 665.

[59] Yang, Wenguang, Xiaowen Wang, Zhen Wang, Wenfeng Liang, and Zhixing Ge. "Light-powered microrobots: Recent progress and future challenges." *Optics and Lasers in Engineering* **161**, (2023): 107380.

[60] Sun, Lingyu, Yunru Yu, Zhuoyue Chen, Feika Bian, Fangfu Ye, Lingyun Sun, and Yuanjin Zhao. "Biohybrid robotics with living cell actuation." *Chemical Society Reviews* **49**, no. 12 (2020): 4043-4069.

[61] Feinberg, Adam W. "Biological soft robotics." *Annual review of biomedical engineering* **17** (2015): 243-265.
[62] Sun, Lingyu, Yunru Yu, Zhuoyue Chen, Feika Bian, Fangfu Ye, Lingyun Sun, and Yuanjin Zhao. "Biohybrid robotics with living cell actuation." *Chemical Society Reviews* **49**, no. 12 (2020): 4043-4069.
[63] Darnton, Nicholas, Linda Turner, Kenneth Breuer, and Howard C. Berg. "Moving fluid with bacterial carpets." *Biophysical journal* **86**, no. 3 (2004): 1863-1870.
[64] Yuan, Hao, Xiaoxia Liu, Liying Wang, and Xing Ma. "Fundamentals and applications of enzyme powered micro/nano-motors." *Bioactive Materials* 6, no. 6 (2021): 1727-1749.
[65] Zhou, Huaijuan, Carmen C. Mayorga-Martinez, Salvador Pané, Li Zhang, and Martin Pumera. "Magnetically driven micro and nanorobots." *Chemical Reviews* **121**, no. 8 (2021): 4999-5041.
[66] Erb, Randall M., Joshua J. Martin, Rasam Soheilian, Chunzhou Pan, and Jabulani R. Barber. "Actuating soft matter with magnetic torque." *Advanced Functional Materials* **26**, no. 22 (2016): 3859-3880.
[67] Rikken, Roger SM, Roeland JM Nolte, Jan C. Maan, Jan CM van Hest, Daniela A. Wilson, and Peter CM Christianen. "Manipulation of micro-and nanostructure motion with magnetic fields." *Soft matter* **10**, no. 9 (2014): 1295-1308.
[68] Cao, Quanliang, Qi Fan, Qi Chen, Chunting Liu, Xiaotao Han, and Liang Li. "Recent advances in manipulation of micro-and nano-objects with magnetic fields at small scales." *Materials Horizons* **7**, no. 3 (2020): 638-666.
[69] Fan, Xinjian, Yihui Jiang, Mingtong Li, Yunfei Zhang, Chenyao Tian, Liyang Mao, Hui Xie, Lining Sun, Zhan Yang, and Metin Sitti. "Scale-reconfigurable miniature ferrofluidic robots for negotiating sharply variable spaces." *Science Advances* **8**, no. 37 (2022): eabq1677.
[70] Sharan, Priyanka, Audrey Nsamela, Sasha Cai Lesher-Pérez, and Juliane Simmchen. "Microfluidics for microswimmers: engineering novel swimmers and constructing swimming lanes on the microscale, a tutorial review." *Small* **17**, no. 26 (2021): 2007403.
[71] Somasundar, Ambika, and Ayusman Sen. "Chemically Propelled Nano and Micromotors in the Body: Quo Vadis?." *Small* **17**, no. 5 (2021): 2007102.
[72] Sharan, Priyanka, Audrey Nsamela, Sasha Cai Lesher-Pérez, and Juliane Simmchen. "Microfluidics for microswimmers: engineering novel swimmers and constructing swimming lanes on the microscale, a tutorial review." *Small* **17**, no. 26 (2021): 2007403.
[73] Wang, Qianqian, and Li Zhang. "External power-driven microrobotic swarm: from fundamental understanding to imaging-guided delivery." *ACS nano* **15**, no. 1 (2021): 149-174.
[74] Edwards, Tara D., and Michael A. Bevan. "Controlling colloidal particles with electric fields." *Langmuir* **30**, no. 36 (2014): 10793-10803.
[75] Cheng, Kunxue, Jiuchuan Guo, Yusheng Fu, and Jinhong Guo. "Active microparticle manipulation: Recent advances." *Sensors and Actuators A: Physical* **322** (2021): 112616.
[76] Al-Ali, Abdulla, Waqas Waheed, Eiyad Abu-Nada, and Anas Alazzam. "A review of active and passive hybrid systems based on Dielectrophoresis for the manipulation of microparticles." *Journal of Chromatography A*, (2022): 463268.
[77] Alekseev, Gennady V., and Dmitry A. Tereshko. "Particle swarm optimization-based algorithms for solving inverse problems of designing thermal cloaking and shielding devices." *International Journal of Heat and Mass Transfer* **135** (2019): 1269-1277.

[78] Chen, Jiajie, Jacky Fong-Chuen Loo, Dongping Wang, Yu Zhang, Siu-Kai Kong, and Ho-Pui Ho. "Thermal optofluidics: principles and applications." *Advanced Optical Materials* **8**, no. 1 (2020): 1900829.

[79] Xiao, Yaxuan, Jinhua Zhang, Bin Fang, Xiong Zhao, and Nanjing Hao. "Acoustics-actuated microrobots." *Micromachines* **13**, no. 3 (2022): 481.

[80] Rao, K. Jagajjanani, Fei Li, Long Meng, Hairong Zheng, Feiyan Cai, and Wei Wang. "A force to be reckoned with: a review of synthetic microswimmers powered by ultrasound." *Small* **11**, no. 24 (2015): 2836-2846.

[81] Grier, David G. "A revolution in optical manipulation." *nature* 424, no. 6950 (2003): 810-816.

[82] Minin, I. V., O. V. Minin, Yu E. Geints, E. K. Panina, and A. Karabchevsky. "Optical manipulation of micro-and nanoobjects based on structured mesoscale particles: a brief review." *Atmospheric and Oceanic Optics* **33**, (2020): 464-469.

[83] Stevenson, David James, Frank Gunn-Moore, and Kishan Dholakia. "Light forces the pace: optical manipulation for biophotonics." *Journal of biomedical optics* **15**, no. 4 (2010): 041503-041503.

[84] Bunea, Ada-Ioana, Daniele Martella, Sara Nocentini, Camilla Parmeggiani, Rafael Taboryski, and Diederik S. Wiersma. "Light-powered microrobots: challenges and opportunities for hard and soft responsive microswimmers." *Advanced Intelligent Systems* **3**, no. 4 (2021): 2000256.

[85] Huang, Tao, Vyacheslav Misko, Anja Caspari, Alla Synytska, Bergoi Ibarlucea, Franco Nori, Jürgen Fassbender, Gianaurelio Cuniberti, Denys Makarov, and Larysa Baraban. "Electrokinetic Janus micromotors moving on topographically flat chemical patterns." *Communications Materials* **3**, no. 1 (2022): 60.

[86] Ceylan, Hakan, Joshua Giltinan, Kristen Kozielski, and Metin Sitti. "Mobile microrobots for bioengineering applications." *Lab on a Chip* **17**, no. 10 (2017): 1705-1724.

[87] Chen, Jiajie, Jacky Fong-Chuen Loo, Dongping Wang, Yu Zhang, Siu-Kai Kong, and Ho-Pui Ho. "Thermal optofluidics: principles and applications." *Advanced Optical Materials* **8**, no. 1 (2020): 1900829.

[88] Jones, Steven, Daniel Andrén, Pawel Karpinski, and Mikael Käll. "Photothermal heating of plasmonic nanoantennas: Influence on trapped particle dynamics and colloid distribution." *ACS Photonics* **5**, no. 7 (2018): 2878-2887.

[89] Jones, Steven, Daniel Andrén, Tomasz J. Antosiewicz, Alexander Stilgoe, Halina Rubinsztein-Dunlop, and Mikael Käll. "Strong transient flows generated by thermoplasmonic bubble nucleation." *ACS nano* **14**, no. 12 (2020): 17468-17475.

[90] Hoekstra, Davey C., Koen Nickmans, Johan Lub, Michael G. Debije, and Albert PHJ Schenning. "Air-curable, high-resolution patternable oxetane-based liquid crystalline photonic films via flexographic printing." *ACS applied materials & interfaces* **11**, no. 7 (2019): 7423-7430.

[91] Lahikainen, Markus, Kim Kuntze, Hao Zeng, Seidi Helantera, Stefan Hecht, and Arri Priimagi. "Tunable photomechanics in diarylethene-driven liquid crystal network actuators." *ACS Applied Materials & Interfaces* **12**, no. 42 (2020): 47939-47947.

[92] Luo, Peng-Fei, Shi-Li Xiang, Chong Li, and Ming-Qiang Zhu. "Photomechanical polymer hydrogels based on molecular photoswitches." *Journal of Polymer Science* **59**, no. 20 (2021): 2246-2264.

[93] Herath, Madhubhashitha, Jayantha Epaarachchi, Mainul Islam, Liang Fang, and Jinsong Leng. "Light activated shape memory polymers and composites: A review." *European Polymer Journal* **136**, (2020): 109912.

[94] Yu, Shimin, Yang Cai, Zhiguang Wu, and Qiang He. "Recent progress on motion control of swimming micro/nanorobots." *View* **2**, no. 5 (2021): 20200113.

[95] Chiou, Pei Yu, Aaron T. Ohta, and Ming C. Wu. "Massively parallel manipulation of single cells and microparticles using optical images." *Nature* **436**, no. 7049 (2005): 370-372.

[96] Zhang, Shuailong, Mohamed Elsayed, Ran Peng, Yujie Chen, Yanfeng Zhang, Jiaxi Peng, Weizhen Li et al. "Reconfigurable multi-component micromachines driven by optoelectronic tweezers." *Nature communications* **12**, no. 1 (2021): 5349.

[97] Liang, Shuzhang, Yuqing Cao, Yuguo Dai, Fenghui Wang, Xue Bai, Bin Song, Chaonan Zhang, Chunyuan Gan, Fumihito Arai, and Lin Feng. "A versatile optoelectronic tweezer system for micro-objects manipulation: transportation, patterning, sorting, rotating and storage." *Micromachines* **12**, no. 3 (2021): 271.

[98] Zhang, Shuailong, Bingrui Xu, Mohamed Elsayed, Fan Nan, Wenfeng Liang, Justin K. Valley, Lianqing Liu, Qiang Huang, Ming C. Wu, and Aaron R. Wheeler. "Optoelectronic tweezers: a versatile toolbox for nano-/micro-manipulation." *Chemical Society Reviews*, (2022).

[99] Frisch, R. "Experimenteller nachweis des Einsteinschen strahlungsrückstoßes." *Zeitschrift für Physik* **86**, no. 1-2 (1933): 42-48.

[100] Chen, Gui-hua, Mu-ying Wu, and Yong-qing Li. "Pulling and lifting macroscopic objects by light." *arXiv preprint arXiv:2008.04074*, (2020).

[101] Killian, Jessica L., Fan Ye, and Michelle D. Wang. "Optical tweezers: A force to be reckoned with." *Cell* **175**, no. 6 (2018): 1445-1448.

[102] Odian, George. *Principles of polymerization*. John Wiley & Sons, 2004.

[103] Ashkin, Arthur, and James P. Gordon. "Stability of radiation-pressure particle traps: an optical Earnshaw theorem." *Optics letters* **8**, no. 10 (1983): 511-513.

[104] Roichman, Yohai, Bo Sun, Yael Roichman, Jesse Amato-Grill, and David G. Grier. "Optical forces arising from phase gradients." *Physical review letters* **100**, no. 1 (2008): 013602.

[105] Simpson, N. B., K. Dholakia, L. Allen, and M. J. Padgett. "Mechanical equivalence of spin and orbital angular momentum of light: an optical spanner." *Optics letters* **22**, no. 1 (1997): 52-54.

[106] Bishop, Alexis I., Timo A. Nieminen, Norman R. Heckenberg, and Halina Rubinsztein-Dunlop. "Optical microrheology using rotating laser-trapped particles." *Physical Review Letters* **92**, no. 19 (2004): 198104.

[107] Lehmuskero, Anni, Robin Ogier, Tina Gschneidtner, Peter Johansson, and Mikael Käll. "Ultrafast spinning of gold nanoparticles in water using circularly polarized light." *Nano letters* **13**, no. **7** (2013): 3129-3134.

[108] Lehmuskero, Anni, Peter Johansson, Halina Rubinsztein-Dunlop, Lianming Tong, and Mikael Kall. "Laser trapping of colloidal metal nanoparticles." *ACS nano* **9**, no. 4 (2015): 3453-3469.

[109] Andrén, Daniel, Denis G. Baranov, Steven Jones, Giovanni Volpe, Ruggero Verre, and Mikael Käll. "Microscopic metavehicles powered and steered by embedded optical metasurfaces." *Nature Nanotechnology* **16**, no. 9 (2021): 970-974.

[110] Wu, Xiaofei, Raphael Ehehalt, Gary Razinskas, Thorsten Feichtner, Jin Qin, and Bert Hecht. "Light-driven microdrones." *Nature Nanotechnology* **17**, no. 5 (2022): 477-484.

[111] Tanaka, Yoshito Y., Pablo Albella, Mohsen Rahmani, Vincenzo Giannini, Stefan A. Maier, and Tsutomu Shimura. "Plasmonic linear nanomotor using lateral optical forces." *Science Advances* **6**, no. 45 (2020): eabc3726.

[112] Sullivan, Dennis M. *Electromagnetic simulation using the FDTD method*. John Wiley & Sons, 2013.

Paper I

Light-driven transport of microparticles with phase-gradient Metasurfaces

Mohammad Mahdi Shanei, Einstom Engay, and Mikael Käll

Optics Letters **47**, 6428-6431 (2022).

Optics Letters

Light-driven transport of microparticles with phase-gradient metasurfaces

Mohammad Mahdi Shanei, Einstom Engay, and Mikael Käll*

Department of Physics, Chalmers University of Technology, 412 96 Gothenburg, Sweden
**Corresponding author: mikael.kall@chalmers.se*

Received 18 October 2022; revised 17 November 2022; accepted 17 November 2022; posted 21 November 2022; published 14 December 2022

Optical tweezers have opened numerous possibilities for precise control of microscopic particles for applications in life science and soft matter research and technology. However, traditional optical tweezers employ bulky conventional optics that prevents construction of compact optical manipulation systems. As an alternative, we present an ultrathin silicon-based metasurface that enables simultaneous confinement and propulsion of microparticles based on a combination of intensity and phase-gradient optical forces. The metasurface is constructed as a water-immersion line-focusing element that enables trapping and transport of 2 μm particles over a wide area within a thin liquid cell. We envisage that the type of multifunctional metasurfaces reported herein will play a central role in miniaturized optical sensing, driving, and sorting of microscopic objects, such as cells or other biological entities.

https://doi.org/10.1364/OL.478179

Introduction. Contactless optomechanical manipulation of microparticles has found numerous applications in biophotonics [1], biomedical research [2], and colloidal sciences [3]. The intensity gradient force achieved by a tightly focused laser beam has an indispensable role in microparticle optical manipulation [4]. However, while a trapped particle can be transported by the spatial displacement and/or tuning of an optical intensity gradient profile, it is challenging to propel numerous particles over a large area [1]. To tackle this challenge, structured beams equipped with phase gradients have been employed to realize all-optical sorting, separation, and transport of multiple particles [5–7]. A phase gradient can steer the direction of light scattering to induce transverse optical forces, which thus adds a complementary degree of freedom in the optical manipulation of microparticles [8]. Various optical elements, such as waveguides [9], tunable q-plates [10], and digital micromirror devices (DMDs) [11] have been used to realize such structured optical patterns. Holographic optical tweezers (HOT) are the most versatile method to generate dynamic optical trapping [12,13]. A spatial light modulator (SLM) with a high numerical aperture (NA) microscope objective is required to implement HOTs, but the bulky nature of this solution unfortunately prevents the construction of really compact optical manipulation systems.

A number of works have addressed the problem of integrating optical force manipulation into compact systems; examples include methodologies based on optical waveguides [14], plasmonic structures [15], coupled cavities [16], optical resonators [17], and freeform focusing reflectors [18]. One of the most recent and promising developments in this direction involves the use of optical metasurfaces [19–25], that is, dense arrays of subwavelength scatterers patterned in a two-dimensional (2D) optically thin layer. By careful design, a metasurface can allow almost full control of light propagation through local modulation of the phase, amplitude, and/or polarization of an incident light wave, all in an extremely compact format [26]. In this work, we describe and discuss a line-focusing dielectric metasurface equipped with a linear phase gradient. The basic idea is to utilize the intensity gradient across the focal line to confine particles, while the phase gradient along the line provides the in-plane momentum necessary to propel the particles in one direction [27]. Our work comprises a first demonstration of transporting multiple particles over a wide area using a metasurface-based system. With a significantly reduced footprint, the system allows for the direct integration of contactless particle manipulation with microfluidic devices.

Metasurface design. Figure 1 illustrates the working principle of a phase-gradient cylindrical metalens immersed in water containing a diluted solution of microparticles. The metalens is designed based on the Pancharatnam–Berry (PB) or geometric phase approach such that a circularly polarized incident plane wave generates a cross-polarized output that focuses into a line while simultaneously providing a linear phase gradient along that line. The metasurface is optimized for an operating wavelength of $\lambda = 1064$ nm and is composed of nanofins made of amorphous silicon (a-Si) periodically arranged in a square lattice on a fused silica (SiO_2) substrate, as shown in the inset of Fig. 1. Each nanofin can be considered as a truncated waveguide supporting localized polarization-dependent electromagnetic resonances. Due to shape birefringence, the cross-polarized output attains a phase delay that is twice the nanofin rotational angle. Thus, by spatially varying the nanofin angular orientations, a 2D phase distribution corresponding to the wanted structured light field can be imprinted on the incident wave.

Optimization of metasurface structure parameters were performed using finite-difference time-domain (FDTD) (Lumerical) electrodynamics simulations with periodic boundary

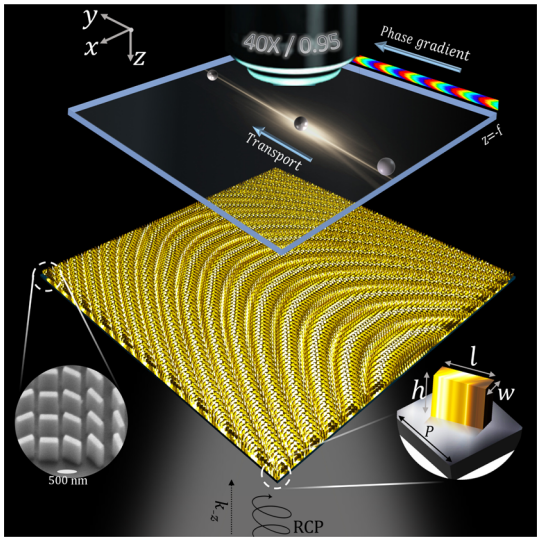

Fig. 1. Working principle of the phase-gradient cylindrical metalens with an ability to optically trap microparticles in a line-focus against the plane located at $z = f$ and simultaneously transporting these particles in one direction along the line-focus. The left-hand inset shows a scanning electron microscope (SEM) image of meta-atoms and the right-hand inset shows the building block of the metasurface, that is, an a-Si nanofin on a SiO_2 substrate.

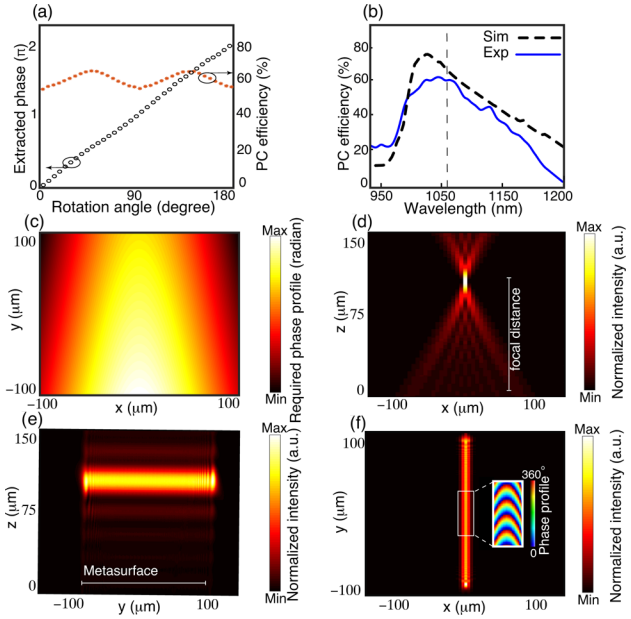

Fig. 2. (a) Extracted phase-shift φ and PCE as a function of nanofin rotation angle for $P = 600$ nm. (b) Experimental and calculated PCE for a uniform array of nanofins oriented at $\varphi = 90°$ as a function of incident wavelength. The dashed vertical line indicates the laser wavelength used in the particle manipulation experiments. (c) Phase profile of the metasurface for $f = 85$ μm and $q = 10$, corresponding to $\theta = 7.5°$. (d)–(f) Fourier simulations of the intensity distribution within the (d) x–z, (e) y–z, and (f) x–y planes. The inset in (f) shows the phase profile within the line focus.

conditions. The plane wave source was set to right circularly polarized (RCP) and a parametric sweep was carried out to find a set of nanofin unit cell parameters with optimized polarization-conversion efficiency (PCE) to left circularly polarized (LCP), yielding a nanofin width $w = 150$ nm, length $l = 490$ nm, and height $h = 500$ nm for a periodicity $P = 600$ nm (see Supplement 1 for details). The same optimization process was implemented for $P = 375$ nm and yielded $w = 160$ nm, $l = 275$ nm, and $h = 500$ nm. However, succeeding discussions in the paper are mainly focused on metasurfaces with $P = 600$ nm. To verify that the optimized structure can introduce up to 2π phase shift, the complex transmittance versus nanofin angular orientation was calculated. Figure 2(a) shows that 0°–180° nanofin rotation indeed allows for full 0–2π phase shift, φ, coverage. The calculated φ acquired by the LCP output was found to be very close to twice the nanofin rotation angle, as expected from the geometric phase concept, while the PCE was maintained around 65% for all orientations. Simulated and experimentally measured efficiency spectra for the optimized structure are shown in Fig. 2(b) as a function of incident wavelength, with approximately 60% PCE for the experimental measurement. The optical characterization setup is detailed in Supplement 1.

To generate a line focus able to both trap and propel microparticles, the metasurface was designed to introduce a spatially varying phase shift given by

$$\phi(x, y) = \frac{2\pi}{\lambda_{\text{eff}}}\left(f - \sqrt{x^2 + f^2}\right) + \frac{2\pi}{qP}y, \tag{1}$$

where $\lambda_{\text{eff}} = \lambda/n$ is the effective wavelength in water with $n = 1.33$, f is the focal length of the metasurface, and x and y are the spatial coordinates. The first term in Eq. (1) is a parabolic phase profile that focuses the incident wave into a line in the x–z plane, yielding an intensity-gradient trapping force, while the second term introduces the linear phase-gradient needed to propel the particles in the y direction. The latter term corresponds to an angular deflection of the transmitted beam, and manifests as a laterally displaced line focus at the focal plane of the metasurface. From the generalized Snell's law, the transmitted beam's angular displacement in the y direction is $\theta = \sin^{-1}(\frac{\lambda_{\text{eff}}}{qP})$ for normal incidence.

Results and discussion. In the following, we concentrate on cylindrical metalenses with focal length $f = 85$ μm, which are suitable for trapping near the bottom of a thin liquid cell adapted for observation using an inverted optical microscope. Using a simplified Fourier optics approach (see Supplement 1), we first calculated intensity and phase maps in the focal plane by discretizing Eq. (1) in a square grid with period P and using the complex transmittances obtained from the FDTD simulations in Fig. 2 as input. To provide maximum in-plane momentum and particle movement, the deflection angle θ should in principle be as high as possible. However, the Fourier simulations revealed that high deflection severely reduces the focusing efficiency of the metalens, and that maximum transverse momentum therefore is achieved at relatively modest deflection angles. Based on this result, and considering fabrication limitations, we settled for $\theta = 7.5°$ ($q = 10$). Figure 2(c) shows the metasurface phase profile corresponding to this case, while Figs. 2(d), 2(e), and 2(f) show the simulated intensity distributions in the x–z, y–z, and x–y planes, respectively. The inset in Fig. 2(f) shows the resulting phase gradient along the line focus required for particle propulsion.

Metasurface performance. In all experimental investigations, the metasurfaces were contained in a closed sample cell

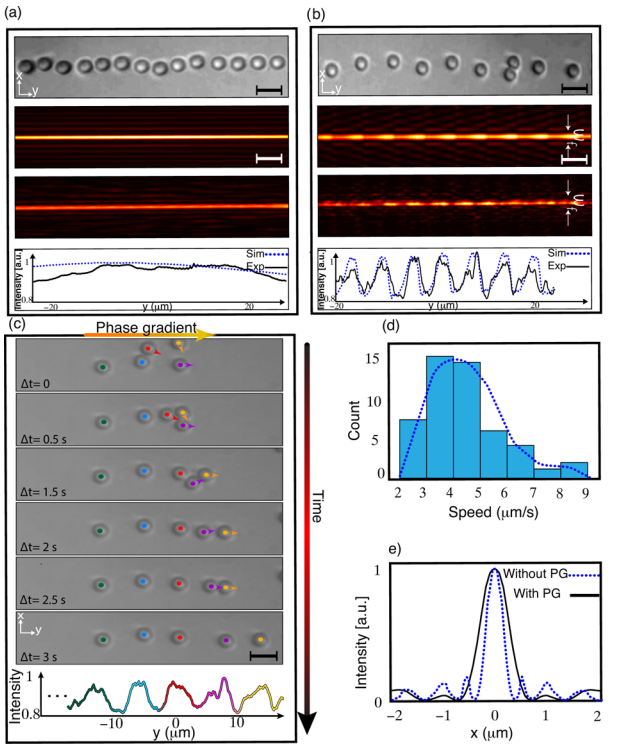

Fig. 3. (a) 2D trapping of the particles at the focal plane ($z = f = 85$ μm) of the metasurface without phase gradient and the simulated and measured intensities along the focal line of the metasurface. (b) 2D trapping of the particles at the focal plane ($z = f = 85$ μm) of the metasurface with around 6 μm spacing for the phase-gradient metasurface with the simulated and measured intensities along the focal line of the metasurface. (c) Snapshots of the motion of the 2D trapped particles at the focal plane of the metasurface with the the local intensity gradients in the last panel. (d) Distribution of the speeds of the particles as they move from one local trap to another. (e) Focal linewidth of fabricated metasurface with and without phase gradient. Scale bars are 5 μm.

containing a dilute solution of 2 μm polystyrene beads dispersed in de-ionized water. The fabrication procedure, optical trapping setup, and SEM images of fabricated structures are shown in Supplement 1.

We first consider a metasurface that only acts as a cylindrical lens, that is, without including the linear phase-gradient term of Eq. (1) in the design. The laser beam enters from the substrate side and excites the metalens, which is in direct contact with the sample solution. The depth of the sample cell is carefully adjusted to coincide with the focal distance, such that particles that sediment or are pushed to the bottom of the well by the radiation pressure can be trapped in 2D (Visualization 1). Figure 3(a) shows that the system enables simultaneous trapping of many particles along the line-focus at the bottom of the sample cell at $z = f = 85$ μm. The bottom subpanels in Fig. 3(a) show uniform profiles in the simulated (middle subpanel) and measured (bottom subpanel) intensities along the focal line of the metasurface. The measured linewidth is found to be ~ 1.2 μm, larger than the expected linewidth for a diffraction-limited metalens but is sufficient enough to ensure stable optical trapping in the x direction as demonstrated in Fig. 3(a).

We next consider a metasurface that also includes the linear phase-gradient term of Eq. (1), that is, with the phase-profile of Fig. 2(c). Particle tracking in videos acquired with a 10× microscope objective revealed three stages of particle motion. First, particles that are initially outside the camera field-of-view move radially toward the center. Then, those particles that are close to the line focus become optically trapped in the x direction. Once trapped, the particles travel in the direction expected from the phase-gradient force (i.e., positive y direction). However, the motion is not smooth but rather consist of irregular jumps triggered by the movement of neighboring particles (see Visualization 2, for an example). To understand this behavior, we first note that before being pushed by the phase-gradient force, the particles tend to localize at well-separated positions, see top subpanel of Fig. 3(b), instead of being almost touching as in Fig. 3(a). It turns out that the particle positions coincide with the locations of intensity hot-spots within the line focus, see bottom three subpanels of Fig. 3(b), that tend to trap particles due to the intensity gradient force. The net result is a series of optical potential wells that are rendered unstable due to the presence of the phase-gradient force, effectively resulting in a trapping landscape similar to a tilted washboard-potential. Thus, if a particle is initially trapped in one of the local hot-spots and a second particle becomes trapped beside it, it is likely that one of them starts to move along the line focus. This is demonstrated, for example, by the particles labeled in orange, red, and purple in Fig. 3(c) (further examples are found in Visualization 2). The average particle speed ($N = 48$) in moving from one local trap to another is found to be ~ 4.3 μm/s for an incident intensity of ~ 3.9 μW μm^{-2}, but show a considerable variation, see Fig. 3(d). We point out that the intensity hot-spots are directly linked to the linear phase gradient, which is obvious from the fact that their separation, ~ 6 μm, coincide with the spatial period qP of the blazed grating term in Eq. (1). As further detailed in Supplement 1, they appear due to deviations from perfectly uniform amplitude transmittance and complete phase-coverage of the meta-atoms, combined with the effect of discretizing the overall phase profile in the y direction. These effects also result in a slight increase of the linewidth to ~ 1.85 μm [see Fig. 3(e)], but this has little influence on the trapping efficiency in the x direction.

To explore the possibility of decreasing the influence of the intensity hotspots by simply defocusing the metalens, we numerically investigated intensity and phase distributions in various z planes beyond the actual focal plane. Figure 4(a) shows an example for $z = f + 10 = 95$ μm. The simulation reveals a set of parallel lines, due to diffraction effects, but with relatively smooth intensity distribution and preserved phase gradient along y. To test the particle trapping and propulsion capabilities in reality, we integrated the same kind of metasurface as above with a sample cell with a depth of approximately 95 μm. Figure 4(b) shows the measured intensity distribution at the bottom of the cell for this case. The snapshots in Fig. 4(c) track two particles as they are propelled within the two line traps. Importantly, we also observe smoother movement of the particles along parts of the tracks. The average particle speeds along the two lines are approximately the same: $v = 2.5$ μm/s for $I = 4$ μW μm^{-2} and linearly dependent on applied intensity, see Fig. 4(d) and Visualization 3. Figure 4(e) shows the resulting individual tracks of particles over a field-of-view of 130 μm × 130 μm. The overall particle dynamics is found to be similar to the case when the focal plane coincide with the bottom of the cell, that is, particles move toward the center, become trapped, and are then propelled in the direction of the phase gradient [see Fig. 4(f)]. Significant

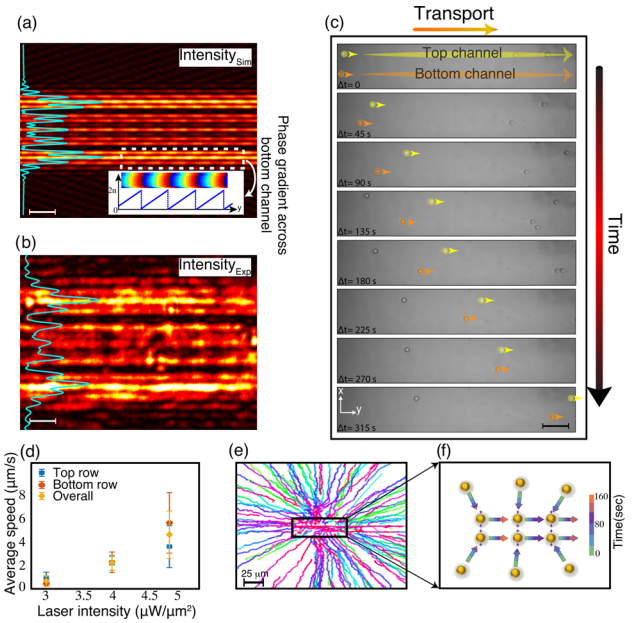

Fig. 4. (a) Simulated intensity profile at $z = f + 10\ \mu m$ with the phase profile in the inset. (b) Measured intensity profile at the trapping plane. (c) Snapshot tracks of particles showing their movement in two channels. (d) Average particles speed in both lines as function of the incident intensity. (e) Displacement of the particles and (f) schematic of the movement of the particles based on the snapshots in (c) with the time scale. Scale bars are 5 μm.

improvements in terms of particle speed and continuous flow can be made by varying the metasurface design parameters. For example, decreasing the meta-atom periodicity to $P = 375$ nm and setting $q = 7$ results in a beam angular displacement of $\theta = 17.7°$, which is close to the optimal deflection angle for maximum transfer of in-plane momentum to the particles for $P = 375$ nm [see Supplement 1, Fig. S4(a)]. Utilizing such a metasurface for particle propulsion along two line traps, the average speed obtained is 12.4 μm/s for $I = 4.8\ \mu W\ \mu m^{-2}$, and a continuous movement of the particles is observed as shown in Visualization 4.

Conclusions. The concept of driving microparticles along well-defined tracks is well-known from previous studies of optical manipulation in structured light-fields constructed using conventional optical components. Though essentially static by nature, metasurfaces can in principle achieve the same functionality in a miniaturized format. In this work, we demonstrated a water-immersion all-dielectric phase-gradient metasurface able to trap and propel microparticles along straight lines and over the length of the focal line, 200 μm. The device was designed based on the geometrical phase approach, using Si nanofins in a square grid as the basic unit, and the maximum transport range, given by the overall extension of the metasurface, corresponded to a typical field-of-view of an optical microscope. Though the effect could be countered by defocusing, we found that the phase gradient responsible for propulsion along a line also caused unwanted intensity fluctuations that tended to lock particles to specific positions. This issue reflects an intrinsic challenge encountered when trying to construct a high-resolution structured light field of similar spatial extension as the metasurface itself based on a grid that is only slightly sub-wavelength in size. Nevertheless, with the current rapid developments in metasurface design methodology, considerable improvement in optical trapping and propulsion efficiency can most likely be achieved.

Funding. Knut och Alice Wallenbergs Stiftelse.

Acknowledgments. This work was performed in part at Myfab Chalmers. We thank Dr. Ruggero Verre and Dr. Daniel Andrén for fruitful discussions.

Disclosures. The authors declare no conflicts of interest.

Data availability. Data underlying the results presented in this paper are not publicly available at this time but may be obtained from the authors upon reasonable request.

Supplemental document. See Supplement 1 for supporting content.

REFERENCES

1. H. Xin, Y. Li, Y.-C. Liu, Y. Zhang, Y.-F. Xiao, and B. Li, Adv. Mater. **32**, 2001994 (2020).
2. S. Corsetti and K. Dholakia, J. Biomed. Opt. **26**, 070602 (2021).
3. D. G. Grier, Curr. Opin. Colloid Interface Sci. **2**, 264 (1997).
4. A. Ashkin, J. M. Dziedzic, J. E. Bjorkholm, and S. Chu, Opt. Lett. **11**, 288 (1986).
5. J. A. Rodrigo and T. Alieva, Optica **2**, 812 (2015).
6. F. Nan and Z. Yan, Nano Lett. **18**, 4500 (2018).
7. J. Rodrigo, M. Angulo, and T. Alieva, Photonics Res. **9**, 1 (2021).
8. Y. Roichman, B. Sun, Y. Roichman, J. Amato-Grill, and D. G. Grier, Phys. Rev. Lett. **100**, 013602 (2008).
9. T. Zhu, A. Novitsky, Y. Cao, M. Mahdy, L. Wang, F. Sun, Z. Jiang, and W. Ding, Appl. Phys. Lett. **111**, 061105 (2017).
10. M. Vergara and C. Iemmi, Phys. Rev. A **100**, 053812 (2019).
11. G. Gauthier, I. Lenton, N. M. Parry, M. Baker, M. Davis, H. Rubinsztein-Dunlop, and T. Neely, Optica **3**, 1136 (2016).
12. J. E. Curtis, B. A. Koss, and D. G. Grier, Opt. Commun. **207**, 169 (2002).
13. G. Volpe, O. M. Maragò, H. Rubinzstein-Dunlop, G. Pesce, A. B. Stilgoe, G. Volpe, G. Tkachenko, V. G. Truong, S. N. Chormaic, F. Kalantarifard, P. Elahi, and M. Käll, "Roadmap for optical tweezers," arXiv arXiv:2206.13789 (2022).
14. C. Pin, J.-B. Jager, M. Tardif, E. Picard, E. Hadji, F. De Fornel, and B. Cluzel, Lab Chip **18**, 1750 (2018).
15. M. L. Juan, M. Righini, and R. Quidant, Nat. Photonics **5**, 349 (2011).
16. C. Renaut, B. Cluzel, J. Dellinger, L. Lalouat, E. Picard, D. Peyrade, E. Hadji, and F. De Fornel, Sci. Rep. **3**, 2290 (2013).
17. S. Lin, E. Schonbrun, and K. Crozier, Nano Lett. **10**, 2408 (2010).
18. S. Yu, J. Lu, V. Ginis, S. Kheifets, S. W. D. Lim, M. Qiu, T. Gu, J. Hu, and F. Capasso, Optica **8**, 409 (2021).
19. G. Tkachenko, D. Stellinga, A. Ruskuc, M. Chen, K. Dholakia, and T. F. Krauss, Opt. Lett. **43**, 3224 (2018).
20. T. Chantakit, C. Schlickriede, B. Sain, F. Meyer, T. Weiss, N. Chattham, and T. Zentgraf, Photonics Res. **8**, 1435 (2020).
21. K. Shen, Y. Duan, P. Ju, Z. Xu, X. Chen, L. Zhang, J. Ahn, X. Ni, and T. Li, Optica **8**, 1359 (2021).
22. O. Ilic and H. A. Atwater, Nat. Photonics **13**, 289 (2019).
23. D. Andrén, D. G. Baranov, S. Jones, G. Volpe, R. Verre, and M. Käll, Nat. Nanotechnol. **16**, 970 (2021).
24. T. Li, X. Xu, B. Fu, S. Wang, B. Li, Z. Wang, and S. Zhu, Photonics Res. **9**, 1062 (2021).
25. X. Li, Y. Zhou, S. Ge, G. Wang, S. Li, Z. Liu, X. Li, W. Zhao, B. Yao, and W. Zhang, Opt. Lett. **47**, 977 (2022).
26. N. Yu and F. Capasso, Nat. Mater. **13**, 139 (2014).
27. Z. Shen, Z. Wang, H. Liu, and Y. Shen, IEEE Photonics J. **12**, 4600810 (2020).

Supplemental Document

Optics Letters

Light-driven transport of microparticles with phase-gradient metasurfaces: supplement

Mohammad Mahdi Shanei, Einstom Engay, and Mikael Käll*

Department of Physics, Chalmers University of Technology, 412 96 Gothenburg, Sweden
**Corresponding author: mikael.kall@chalmers.se*

Supplement DOI: https://doi.org/10.6084/m9.figshare.21596718

Parent Article DOI: https://doi.org/10.1364/OL.478179

Light-driven transport of microparticles with phase-gradient metasurfaces: supplementary information

1. METAATOM OPTIMIZATION

Finite-difference time-domain (FDTD, Lumerical) simulations were performed using plane-wave illumination of single nanofins (metaatoms), with periodic boundary conditions (PBC) implemented on the sides of the unit cell and perfectly matched layers (PML) along the propagation direction. The source was set to be right circularly polarized (RCP) and the complex transmittance of the cross-polarized (left circularly polarized, LCP) output was examined. Complying with the Nyquist sampling rate while ensuring weak interaction between adjacent nanofins and avoiding higher diffraction orders, the unit cell periodicity was set to $P = 600$ nm. Figure S1 (a) shows a parametric sweep used to find the nanofin width (w) and length (l) yielding the highest RCP to LCP polarization conversion efficiency (PCE). Based on fabrication constraints and the results in Fig. S1 (b), the nanofin height was fixed to 500 nm. This resulted in optimized dimensions $w = 150$ nm and $l = 490$ nm for an excitation wavelength of 1064 nm. The aspect ratio of the meta-atoms with the optimized parameters for $P = 600$ nm allowed us to fabricate the nanopillar with sharp edges and vertical side walls.

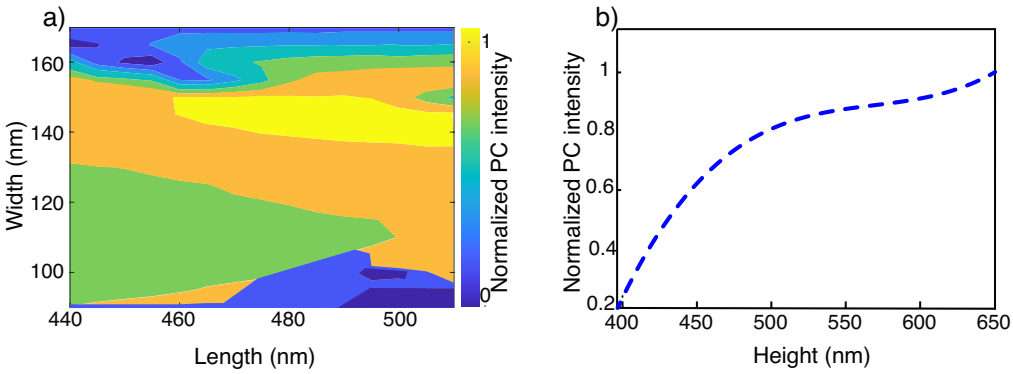

Fig. S1. (a) Normalized polarization conversion efficiency for different nanofin cross-sections. Here, $P = 600$ nm and $h = 500$ nm, for which, the highest efficiency is achieved with $l \times w = 490$ nm $\times$ 150 nm. (b) Normalized PCE as a function of nanofin height.

2. PCE MEASUREMENT

The optical setup used to measure polarization conversion efficiency (PCE) of periodic arrays of nanofins is illustrated in Fig. S2. The sample is placed between orthogonal linear polarizers as indicated. For the case when the nanofins are oriented at 45°, as illustrated by the SEM image in the inset, the array functions as a half-wave plate. The recorded intensity, normalized to the incident intensity, then yields the PCE (58% for the optimized case).

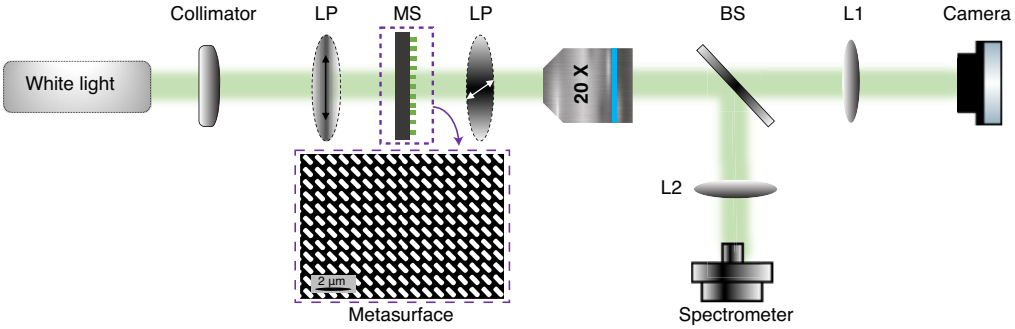

Fig. S2. Optical setup used to measure the PCE of uniform metasurfaces.

3. INTENSITY AND PHASE PROFILE SIMULATIONS

We simulated intensity and phase profiles using the Rayleigh-Sommerfeld diffraction integral applied to a set of discrete source points corresponding to the positions of nanofins in the fabricated metasurfaces. Figure S3 (a) shows an intensity map at the focal plane of a metasurface with deflection angle 7.5° ($q = 10$) obtained by applying the ideal phase profile (Eq. 1 in the main text) and uniform source point amplitudes. In (b) we have instead used the complex transmittances of each nanofin obtained from FDTD simulations. As shown in Fig. 2 (a) in the main text, these show slightly non-uniform amplitude coefficients versus nanofin rotation angle. Weak intensity fluctuations along the central focal line can now be observed, but there are no distinct hotspots with the same periodicity qP as the phase variation along the line, as is observed in the experiment (Fig. S3 (d)). However, the experimental intensity pattern can be well reproduced if we artificially restrict the phase range imposed by the metasurface. As shown in Fig. S3 (c), where we have set the maximum phase shift introduced to the impinging beam to $5\pi/4$, a restricted phase range results in regularly spaced intensity hot-spots with separation distance determined by the spatial period qP of the blazed grating term in Eq.1. Furthermore, the relative intensity of the hotspots increases as the phase coverage decreases.

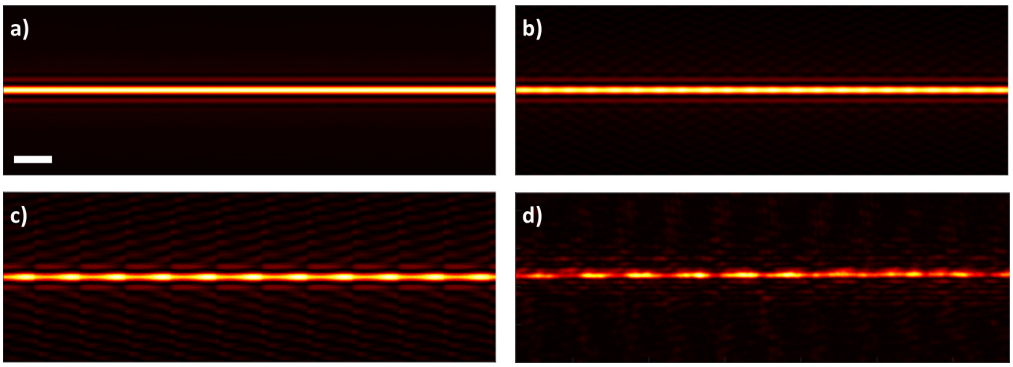

Fig. S3. Simulated local intensity profiles using (a) ideal metasurface profile, (b) metasurface profile rendered using the complex transmittances of the meta-atoms obtained from FDTD, and (c) metasurface profile that introduces a maximum phase shift of $5\pi/4$ compared to experiment (d). Scale bar: 5 µm.

4. OPTIMUM DEFLECTION ANGLE

The phase-gradient force / radiation pressure along the focal line is approximately proportional to the product of sin (θ), where θ is the deflection angle, and the maximum intensity in the line. We calculated intensity profiles for metasurfaces with P = 600 nm based on complex nanofin FDTD transmittances using the Rayleigh-Sommerfeld approach for various θ-values. The results show that the focal line significantly broadens with increasing deflection, resulting in a rapidly decreasing maximum intensity. This is shown in Fig. S4 (a) for two different periodicities of

600 nm and 375 nm, where the intensity has been normalized to $\theta = 0$ (the simple cylindrical metalens). When multiplied by sin (θ), a broad peak at low angles appears. Increasing deflection also results in a shift of the focal distance, see Fig. S4 (b), and pronounced side-lobes around the focal line. By considering these factors, we settled for a deflection angle of $\theta = 7.5°$, which is close to the optimum angle and has a 2-μm focal shift closer to the metasurface plane. This is most suitable for the constructed sample cell used in the optical manipulation experiments.

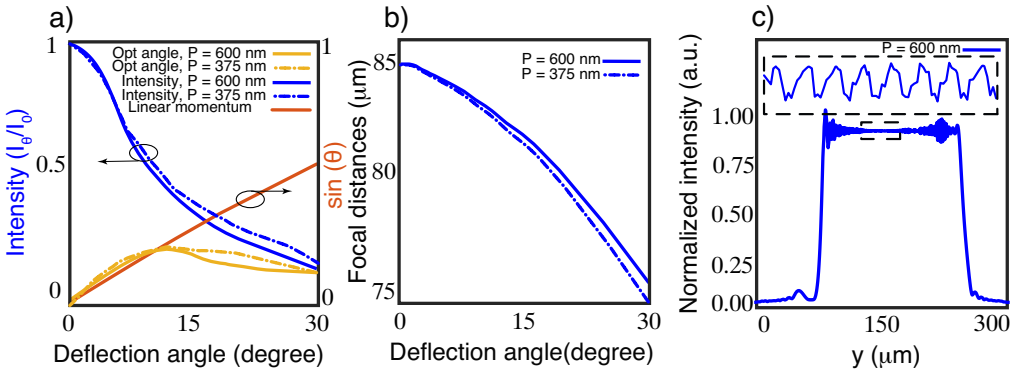

Fig. S4. (a) Optimum deflection angle of the phase gradient metalens to transfer the highest linear in-plane momentum to the particles by considering the trade-off between normalized intensity to and normalized linear momentum for P = 600 nm and P = 375 nm. (b) Axial shifting of focal distance as a function of the deflection angle. (c) Intensity profile at focal plane for the deflection angle of $\theta = 7.5°$ and the fluctuations of the intensity in the inset with the periodicity of 6 μm.

5. SAMPLE PREPARATION AND OPTICAL MANIPULATION SETUP

Figure S5 (a) schematically illustrates the setup used for optical manipulation. The sample cell is formed by the metasurface substrate and a microscope glass slide separated by an adhesive film. The adhesive film is first taped against the glass slide, and the resulting well is filled with a dilute solution of polystyrene beads ($\varnothing = 2$ μm, microParticles GmbH) dispersed in deionized water. The metasurface substrate is then adhered to the other side of the adhesive film. By carefully pushing the metasurface substrate and the glass slide against each other using a micrometer caliper, 85 μm or 95 μm sample cell thickness was achieved. The distance was verified by axially scanning the metasurface plane and the bottom water-glass interface in a microscope. The linearly polarized output of a 1064 nm laser (Cobolt Rumba, beam $\varnothing = 1$ mm) is converted into RCP using a half-wave plate (HWP) and a quarter-wave plate (QWP) and then relayed onto the metasurface using a (de)magnifying 4f configuration ($f_1 = 500$ mm, $f_2 = 100$ mm). A 10/90 (R/T) beam splitter is inserted in the light path to monitor the power incident on the metasurface. The sample cell is mounted on an inverted microscope and imaged in reflection using a white light source, a 40×, NA = 0.9, microscope objective, a removable short-pass filter (SPF), and a CCD camera. A QWP and a polarizer can be inserted in the imaging path to select polarization converted transmission through the metasurface and block background from the laser. Recorded images and videos were postprocessed and analyzed using particle tracking software.

6. METASURFACE FABRICATION

500 nm of amorphous Si (aSi) was deposited on SiO_2 by low-pressure chemical vapor deposition (LPCVD) at 560° C. Ellipsometry measurements showed a refractive index of $n = 3.71$ at 1064 nm. The process continued by 300 nm spin-coating of a negative resist (maN2405, Micro Resist Technology GmbH, Germany). To prevent charging of the substrate, a conductive polymer (Espacer 300Z) was added on top of the resist. An electron beam lithography (Raith EBPG5200) exposure (625 μC/cm^2 with a current of 10 nA) followed, after which the sample was rinsed in water to remove the conductive layer. The pattern was developed for 6 minutes and then transferred to a-Si using reactive ion etching in a HBr plasma (30 sccm HBr, 1.5 mTorr, 230 W).

Finally, the remaining resist was removed by high-power oxygen plasma etching. Figure S5 (b,c) shows an optical image and a SEM image of a fabricated metasurface.

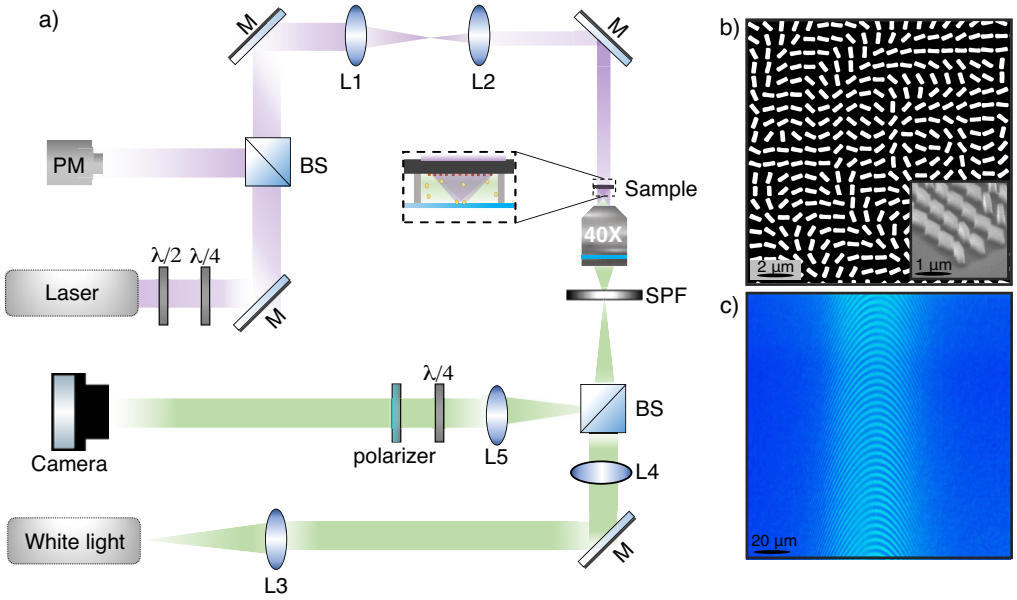

Fig. S5. (a) Optical trapping setup. L1-L5, lenses ($f_1 = 500$ mm, $f_2 = 100$ mm, $f_3 = 50$ mm, $f_4 = 300$ mm, $f_5 = 200$ mm); M, plane mirror; $\lambda/2$, HWP; $\lambda/4$, QWP; BS, beam splitter; SPF, short-pass filter; $40\times$ objective (NA = 0.9); camera (Thorlabs, CCD). (b) SEM image of fabricated metasurface with a tilted view shown in the inset. (c) False color white-light transmission image of a metasurface.